Ref. Ares(2025)5142003 - 27/06/2025
Funded by the European Union
Horizon Europe programme, grant agreement No. 101096068

RETROFIT SOLUTIONS TO ACHIEVE 55% GHG REDUCTION BY 2030

Hydrodynamic optimisation of ships with ALS and relevant response surfaces

WP 2 – Hydrodynamic design optimisation
Task 2.3 – Hydrodynamic optimisation of ships with ALS
D 2.3 – Report on hydrodynamic optimisation of ships with ALS & relevant response surfaces
Partners involved: LJMU, CNR, SFD, NTUA, AALTO
Authors: David Hitchmough, Andrew Spiteri, Onur Yuksel, Viknash Shagar, Eddie Blanco-Davis, Jin Wang, Reuben D'Souza, Vassilios Zagkas, George Papadakis, Kostas Belibasakis

Project details

Project Title	RETROFIT SOLUTIONS TO ACHIEVE 55% GHG REDUCTION BY 2030
Project Type	Innovation Action
Project Acronym	RETROFIT55
Grant Agreement No.	101096068
Duration	36 M
Project Start Date	01/01/2023

Deliverable information

Status (F: final; D: draft; RD: revised draft)	F
Planned delivery date	31/12/2024
Actual delivery date	24/06/2025
• **Dissemination level:** PU – Public, fully open, e.g. web (Deliverables flagged as public will be automatically published in CORDIS project's page) • SEN – Sensitive, limited under the conditions of the Grant Agreement • Classified R-UE/EU-R – EU RESTRICTED under the Commission Decision No2015/444 • Classified C-UE/EU-C – EU CONFIDENTIAL under the Commission Decision No2015/444 Classified S-UE/EU-S – EU SECRET under the Commission Decision No2015/444	PU
Type: Report, Website, Other, Ethics	Report

Document history

Version	Date	Created/Amended by	Changes
01	10/01/2025	David Hitchmough (LJMU)	First Draft
02	24/02/2025	Emanuele Spinosa (CNR)	Revision
03	07/03/2025	David Hitchmough (LJMU)	Second Version
04	25/03/2025	David Hitchmough (LJMU)	Third Version
05	11/04/2025	David Hitchmough (LJMU)	Fourth version
06	20/06/2025	David Hitchmough (LJMU)	Fifth version
06	24/06/2025	David Hitchmough (LJMU)	Final version

Quality check review

Reviewer (s)	Main changes / Actions
Andrew Spiteri (LJMU)	Review (Technical and Stylistic changes)
Eddie Blanco-Davis (LJMU)	Review (Technical and Stylistic changes)
Riccardo Broglia (CNR)	Technical review
Emanuele Spinosa (CNR)	General review
Cecilia Leotardi (CNR)	Editorial review
Cecilia Leotardi & Alessandro Iafrati (CNR)	Final review of contents and submission to EC.

Table of Contents

List of figures 5
List of tables....7
List of acronyms....8
Executive Summary....9
1 Introduction 10
1.1 Air lubrication and propulsion background....10
2 Principle and formulation for the propulsive characteristics 12
3 Air-water stream....13
3.1 Assumptions for the air-water stream model 13
3.2 CFD approach for the air-water stream model....13
3.3 Domain discretisation and simulation setup....14
3.3.1 Computational grid 14
3.4 Results for the air-water stream cases 15
4 Injection through a slit with the use of a plate 17
4.1 CFD simulation details....18
4.2 Domain and meshing....19
4.3 Single-phase simulation baseline 22
4.4 Multi-phase results....23
4.5 As designed multi-phase cases....23
4.6 Increased air cases....28
4.7 Increased air and water cases....34
4.8 Supplementary pure air cases 40
5 Response surface methodology and input to surrogate models 43
5.1 Contour plots 43
5.2 Surface plots....45
5.3 Factorial plots 47
6 Concluding remarks....48
References 50
Appendix 1 – Relative parameters....51

List of figures

Figure 1: Schematic representation of the computational model employed. 13
Figure 2: Mesh visualization. 15
Figure 3: Blade thrust coefficient, torque coefficient and the efficiency grade over the advance coefficient. 16
Figure 4: RETROFIT55 propeller density and pressure visualizations using mixed inlet at J = 0.7. 16
Figure 5: Plate geometry showing the location of the tapered slit. 17
Figure 6: Representation of the ‘bullet-shaped’ domain. 19
Figure 7: Rotating region in relation to the plate. 20
Figure 8: Representation of the mesh around the propeller. 20
Figure 9: Underside of the plate mesh. 21
Figure 10: Top of the plate mesh. 22
Figure 11: Plot of the y+ value on the propeller. 23
Figure 12: Thrust coefficient, torque coefficient, and Kt/10Kq for the ‘As Designed’ condition. 24
Figure 13: Volume fraction of air scene for the ‘As Designed’ condition (0.997 m/s case). 25
Figure 14: High contrast image 1 for the ‘As Designed’ condition (0.997 m/s case). 25
Figure 15: High contrast image 2 for the ‘As Designed’ condition (0.997 m/s case). 26
Figure 16: Volume fraction of air on the propeller geometry for the ‘As Designed’ condition (0.997 m/s case). 26
Figure 17: Volume fraction of air scene for the ‘As Designed’ condition (1.169 m/s case). 27
Figure 18: High contrast image 1 for the ‘As Designed’ condition (1.169 m/s case). 27
Figure 19: High contrast image 2 for the ‘As Designed’ condition (1.169 m/s case). 27
Figure 20: Volume fraction of air on the propeller geometry for the ‘As Designed’ condition (1.169 m/s case). 28
Figure 21: Increased air results for 0.894 m/s. 29
Figure 22: Increased air results for 0.997 m/s. 29
Figure 23: Increased air results for 1.066 m/s. 30
Figure 24: Increased air results for 1.169 m/s. 30
Figure 25: Volume fraction of air scene for the 0.997 m/s case 2 set-up. 32
Figure 26: High contrast image for the 0.997 m/s case 2 set-up. 32
Figure 27: Volume fraction of air on the propeller geometry for the 0.997 m/s case 2 set-up. 32
Figure 28: Volume fraction of air scene for the 1.169 m/s case 1 set-up. 33
Figure 29: High contrast image for the 1.169 m/s case 1 set-up. 33
Figure 30: Volume fraction of air on the propeller geometry for the 1.169 m/s case 1 set-up. 33
Figure 31: Increased air and water results for 0.894 m/s. 35
Figure 32: Increased air and water results for 0.997 m/s. 35
Figure 33: Increased air and water results for 1.066 m/s. 36
Figure 34: Increased air and water results for 1.169 m/s. 36
Figure 35: Volume fraction of air scene for the 0.997 m/s case 7 set-up. 37
Figure 36: High contrast image for the 0.997 m/s case 7 set-up. 38
Figure 37: Volume fraction of air on the propeller geometry for the 0.997 m/s case 7 set-up. 38
Figure 38: Volume fraction of air scene for the 1.169 m/s case 10 set-up. 38
Figure 39: High contrast image for the 1.169 m/s case 10 set-up. 39
Figure 40: Volume fraction of air on the propeller geometry for the 1.169 m/s case 10 set-up. 39
Figure 41: Pure air injection results for 1.169 m/s. 40

Figure 42: Volume fraction of air scene for the 0.05 kg/s case. 41
Figure 43: High contrast image for the 0.05 kg/s case. 41
Figure 44: Volume of fraction of air on the propeller geometry for the 0.05 kg/s case. 42
Figure 45: Contour plot of relative change in thrust coefficient vs relative rate of water flow and relative velocity. 44
Figure 46: Contour plot of relative change in thrust coefficient vs relative rate of air flow and relative velocity. 44
Figure 47: Contour plot of relative change in thrust coefficient vs relative rate of air flow and relative rate of water flow. 45
Figure 48: Surface plot of relative change in thrust coefficient vs relative rate of water flow and relative velocity. 46
Figure 49: Surface plot of relative change in thrust coefficient vs relative rate of air flow and relative velocity. 46
Figure 50: Surface plot of relative change in thrust coefficient vs relative rate of air flow and relative rate of water flow. 46
Figure 51: Main effects plot for relative change in thrust coefficient. 47

List of tables

Table 1: Baseline propeller thrust and torque data. 22
Table 2: 'As designed' condition results. 24
Table 3: Increased air cases. 28
Table 4: Volume fractions and combined mass flow rates for the increased air cases. 28
Table 5: Increased air and water cases. 34
Table 6: Volume fractions and combined mass flow rates for the increased air cases. 34
Table 7: Regression equation coefficients. 43

List of acronyms

ALS	Air Lubrication System
CFD	Computational Fluid Dynamics
CNR	Consiglio Nazionale Delle Ricerche
CO2	Carbon Dioxide
DES	Detached Eddie Simulations
EU	European Union
GHG	Green House Gas
HPC	High-Performance Computing
ITTC	International Towing Tank Committee
JBC	Japanese Bulk Carrier
LES	Large Eddie Simulations
LJMU	Liverpool John Moores University
MPI	Message Passing Interface
NOx	Nitrogen Oxides
NTUA	National Technical University of Athens
PALS	Passive Air Lubrication System
RANS	Reynolds-Averaged Navier Stokes
RANSE	Reynolds-Averaged Navier Stokes Equations
RPM	Rotations per Minute
SA	Spalart Allmaras
SOx	Sulphur Oxides
URANS	Unsteady Reynolds-Averaged Navier Stokes
VOF	Volume of Fluid
WMF	World Merchant Fleet

Executive Summary

This report considers the potential impact of air ingress resulting from using a Passive Air Lubrication (PALS) System on ship propeller characteristics. The PALS system introduces air into the near-wall region of a vessel, and the skin friction on the wall can be reduced. The reduction in skin friction can improve fuel efficiency and help to reduce emissions. Air lubrication has positioned itself as one of the most promising decarbonisation technologies currently available to the maritime industry. However, the potential impact of air ingress on propulsive characteristics is poorly understood. Should air ingress significantly affect the propeller, this must be given appropriate consideration within the overall business case for the technology. This may require design and operational changes or impact the general uptake in operator use of the technology.

This report presents the findings of Computational Fluid Dynamics (CFD) simulations, which have been carried out to investigate the impact of air ingress on the propeller. As the simulations are created based on the operation of the PALS (a Venturi system), the air is introduced as a mixture of air and water in most cases and as pure air in the final set of simulations to assess the differences in impact from the injection of pure air. Through the design of the cases, the potential effects of air ingress on the propeller can be taken alongside the beneficial effects of drag reduction. The PALS system developed by ARMADA Technologies produces a mixture of air and water, which will be injected beneath the hull at specific points using custom-designed injectors.

The report considers the introduction of air into the propeller via two different approaches, firstly by injecting the air-water mixture at two ratios, 90% water to 10% air and 95% to 5% air, via the use of a simplified model, to assess the effect of ingress on propeller performance. This first approach could be likened to a stream of water and air being injected into the propeller, and the stream is not affected by the buoyancy effects that would be witnessed with air, instead intersecting with the blade tangentially. Secondly, an alternative approach is used where the air-water mixture is introduced into the domain via a slit in a plate; the air therefore travels along the plate and subsequently flows into the propeller plane. In the second approach, the effects of buoyancy constrain the air against the plate, and this is a closer replication of the air topography and behaviour that may be seen with air lubrication. In the secondary approach, the quantity of air and water is varied by increasing the airflow exclusively and increasing the air and water flow together.

The first and second approaches utilise a VOF method, which considers the two phases immiscible. In reality, the air-water mixture and its behaviour would not follow an immiscible assumption, and this must be considered alongside this work and future comparisons to experimental testing.

1 Introduction

1.1 Air lubrication and propulsion background

The World's Merchant Fleet (WMF), with 58,000 ships, is responsible for 3% of global GHG emissions. As a country, it would be the sixth largest polluter. WMF is under massive legislative, economic, and commercial pressure to reduce emissions. WMF adoption of zero-carbon fuels will take several decades, cost over $1 trillion, and deliver significantly less energy/tonne vs. hydrocarbons.

Air injection introduces air into a vessel's boundary layer, modifying its density, wetted surface area, viscosity, turbulence viscosity, and wall shear. The combination of these effects results in an observable reduction in drag. However, understanding these effects in isolation and their broader impact on seakeeping parameters remains a point still awaiting sufficient investigation. In many Air Lubrication Systems (ALS), the air injected into the boundary layer must be done via a compressor with a corresponding powering requirement. The powering requirement will either reduce the overall net saving from using ALS or, in the worst case, negate any saving, possibly even increasing the powering requirement. A further consideration arising from ALS is the quantity of air that must be injected for the desired level of drag reduction to be achieved.

Monitored waterborne Carbon Dioxide (CO2) emissions in Europe indicate that shipping releases 144.6 million tons, and inland waterway transport in the European Union (EU) results in around 3.8 million tons of CO2 emissions annually. Furthermore, shipping is responsible for 24% of the EU's Nitrogen oxides (NOx) and Sulphur oxides (SOx) emissions, with very high amounts found in coastal and port areas. With the current regulations, after 2030, NOx emissions from the maritime industry are expected to exceed the EU's land-based sources [1].

The simulation of air lubrication in CFD has advanced considerably in recent decades, alongside increased operator knowledge and computational resources. However, many aspects of the technology have yet to be fully explored, including but not limited to its impact on seakeeping parameters and its drag-reduction mechanism. This work aims to tackle one of the most pertinent and pressing questions regarding air lubrication: its effects on seakeeping parameters, specifically its impact on the propeller and the propeller's propulsive characteristics. Sufficient modelling of the multiphase scenario is necessary for investigating the injected air's effect on seakeeping and propulsive characteristics, which is further accentuated by the presence of the propeller in the simulation. The propeller creates a highly turbulent mixing region for the continua fluid and the dispersed air in the propeller plane.

Extensive research has been conducted on the technology since the 1970s. Research was undertaken on the applicability of bubbly flows for gas-based lubrication systems at the Krylov Shipbuilding Institute from 1961 into the 1970s [2]. Interest was sustained through the 1970s, driven by the ongoing oil crisis and the subsequent desire to identify methods for reducing fuel consumption in shipping. Early investigations of the applicability of using gas-based skin frictional drag reduction methods used hydrogen bubbles generated through electrolysis [3, 4]. Although hydrogen gas behaves differently from air, this still allowed the operators to investigate the effect of gas in the near-wall region of a flat plate and identify some preliminary indicators, such as the point of peak drag reduction, which the authors identified as being immediately after the gas's injection point.

Current CFD approaches, specifically the Volume of Fluid (VOF) method, have limitations when considering dispersed-continuous phase regimes. VOF has, however, seen considerable use in the simulation of free surface scenarios, such as those used in replicating towing tank tests for hull and plate models. The VOF method, although highly applicable to several scenarios, represents the multiphase scenario as two distinct phases with a sharp interface. In the case of a bubbly regime, this assumption would not be sufficient. So, the usefulness of this model is in the simulation of a continuous air layer rather than a bubbly layer.

Research on the effect of air ingress on propeller propulsive performance is relatively limited. Some researchers have considered the impact of the air layer on propeller characteristics for a specific ALS [5], with a specific focus on the void fraction at the propeller and pressure fluctuations. The authors point to the potential for air ingress to alter propeller characteristics, reduce propeller operational efficiency and influence noise generation. Some researchers who have also looked at the impact of air ingress on propeller characteristics have also used VOF two-phase approaches [6]. However, as stated, the VOF model relies on the immiscible two fluids in each control cell, which is a limited assumption. Regardless of the limitations of VOF simulation for this scenario, researchers in these studies have suggested that in the specific cases that they have tested, air did not enter the propeller working area directly. Despite not entering the propeller working area directly, these studies witnessed a reduction in Thrust and Torque coefficient, indicating the potential detrimental effects of air ingress.

This report links to another report under the RETROFIT 55 project, ‘System design to deliver maximum drag reduction by PALS’ [7], which may also interest the reader.

2 Principle and formulation for the propulsive characteristics

The primary propulsive characteristics of interest in propeller simulations are the thrust and torque generated by the propeller. Subsequently, the thrust and torque can be utilised to determine the propeller efficiency. It is theorised that the thrust and torque values will be affected by the introduction of air into the propeller. Investigating these changes will elucidate the impact of air lubrication on ships. So that the thrust and torque may be determined, thrust and torque coefficient reports were created (as well as corresponding monitors and plots). The performance of the propeller is assessed using

- the advance coefficient $J = \frac{V_\infty}{nD}$
- the thrust coefficient $k_T = \frac{T}{\rho_m n^2 D^4}$
- the torque coefficient $k_Q = \frac{Q}{\rho_m n^2 D^5}$
- the propeller efficiency $\eta = \frac{J}{2\pi} \frac{k_T}{k_Q}$

where V_∞ is freestream velocity, n is rotational rate, D is diameter, T is thrust, ρ_m is mixture density and Q is torque.

In addition to considering the propeller's propulsive characteristics, pertinent plots regarding variation in air volume fraction have also been considered to assess air distribution.

It is worth stating that in this report, where the term ‘torque coefficient’ is used, this refers to the value 10*torque coefficient ($10k_Q$).

3 Air-water stream

The first approach undertaken to investigate the impact of air ingress on propeller characteristics uses a simplified model representing the air-water mixture as a stream where the water is mixed with air uniformly at a specified ratio. This ratio contains two nominal values for air and water density, $\rho_a = 1.2\,kg/m^3$ and $\rho_w = 998.2\,kg/m^3$ respectively. Also, the uniform stream is imposed as a boundary condition on a cylindrical region of radius $0.4R \le r \le 0.6R$ and only on the upstream face (fore side of the propeller), from where it propagates and interacts with the blades. In this case, two mixture ratios are considered, namely, 90% (90% water and 10% air) and 95% (95% water and 5% air). A schematic representation can be found in Figure 1.

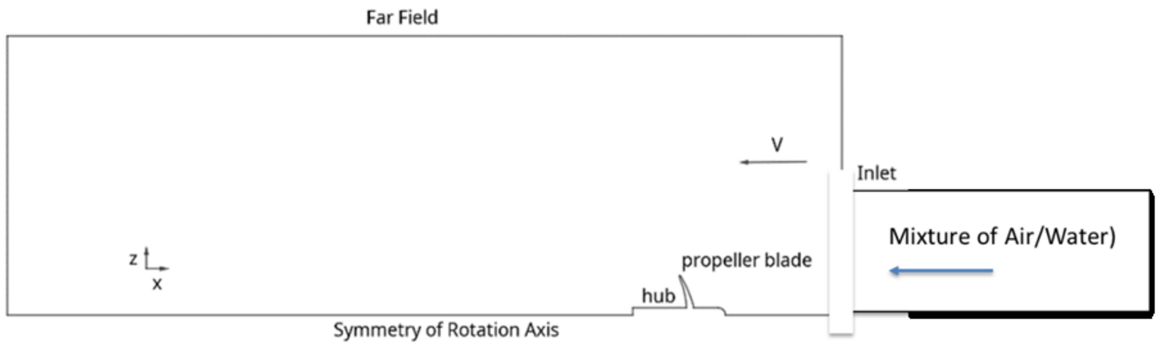

Figure 1: Schematic representation of the computational model employed.

3.1 Assumptions for the air-water stream model

To model such a phenomenon in the context of CFD, we first assume that the mixture is uniform, i.e., it has a constant density of $0.9\rho_{water} + 0.1\rho_{air} = 898.2\ \mathrm{kg}/m^3$. This allows for the use of two-phase modelling based on the volume of fluid (VOF) technique, just as it is used for free-surface flow simulations.

3.2 CFD approach for the air-water stream model

For all the simulations, the MaPFlow code is used. MaPFlow is an unsteady Reynolds-Averaged Navier Stokes (URANS) solver primarily developed at the NTUA [8]. It is a cell-centred CFD Solver that can use both structured and unstructured grids. It can solve compressible flows, as well as fully incompressible flows, using the artificial compressibility method [9]. The convective fluxes are discretised using the approximate Riemann solver of Roe, while a central scheme is employed for the viscous fluxes. Turbulence closures include the turbulence model of Spalart (SA) and the two-equation turbulence model of Menter ($k - \omega\, SST$). Higher fidelity turbulence models are also implemented, including Larger Eddy Simulations (LES) and Detached Eddy simulation (DES) models [10]. Regarding laminar to turbulent transition modelling, two variants are available: the correlation γ-Re_θ model of Menter and the e^n model. Regarding two-phase flows, the Volume of Fluid (VOF) method is coupled with the artificial compressibility formulation [9]. MaPFlow is coupled with a dynamic rigid body solver and a mooring line finite element solver to deal with offshore structures in marine environments [11]. Finally, it is parallelised using the MPI library in a multi-block fashion in which each processor solves a partition of the original computational domain.

MaPFlow's parallel performance has been investigated in various HPC platforms where the scalability of the code up to 64000 processors was verified. Finally, it has been extensively used in AVATAR and INNWIND, SEATECH and RETROFIT55 EU projects.

In this work, the two-equation $k - \omega\, SST$ Reynolds Averaged Navier Stokes Equation (RANSE) model is used for resolving a fully turbulent flow of approximately $Re = 1.6 \cdot 10^8$ Reynolds number at $0.7R$ and nominal advance coefficient of $J = 0.7$. The system is discretised in time using a fully implicit second-order backward difference formula scheme relaxed with the artificial compressibility method. With this method, the simulation is marched in pseudo-time using an artificial speed of propagation numerically calibrated to precondition the system of equations until it reaches steady convergence, i.e., the relative error is adequately small.

3.3 Domain discretisation and simulation setup

The propeller at hand is the RETROFIT55 model, which has a nominal diameter of $D = 6.95\, m$ and consists of 5 blades. Since the propeller has rotational symmetry, we can divide the domain of simulation by the number of blades and simulate only one blade inside a cylindrical slice. The boundary conditions on the radial slices are periodic, which means that boundary values in the halo cells of the first periodic surface are taken from the inner boundary cells of the second. Concerning the far field surfaces, the radial distance of the far field is located at $33\, m$ from the shaft axis, the upwind face is $40\, m$ and the downwind face is $100\, m$ distant from the propeller blade. The grid independence study for the specific propeller was conducted in the Task 2.1 of WP2; consequently, the same characteristics were used with mesh refinement in the jet region.

3.3.1 Computational grid

In terms of blade discretisation, its spanwise cell density is $1\, mm$ at the leading edge and $10\, mm$ at the trailing edge. Also, its chordwise density is (at max) approximately $7\, mm$ at the root of the blade $(0.2R)$ and $4.5\, mm$ at the blunt tip $(1.0R)$. Finally, its maximum cell dimension due to unstructured mesh creation, where the curvature is small, is close to $45\, mm$, and at the (highly curved) region of the leading-edge strip, the chordwise dimension starts from $0.1\, mm$ before its gradual increase. Due to the presence of the (artificial) hub at the fore of the blade, we prefer to subtract its contribution to drag, and therefore, we set the boundary condition to be "slip & no-through".

The specification of the volume mesh near the blade wall follows the y^+ criterion, used for RANSE simulations, in which, for $y^+ = 1$ we obtain a first-cell height $h_1 = 0.0025\, mm$. Far-field cell density at the cylindrical part and aft of the propeller reaches $5\, m$. We should, however, ensure that the mixed jet is clearly defined and well sampled at the input far field. For this reason, we use control cell size boxes of cylindrical type for up to $0.75R$ radius, spanning from the inflow to the surrounding region of the blade. These boxes restrict the cell size to $78\, mm$. The above resulted in a volume mesh of around 12 million cells, while the blade surface mesh comprised around 250 thousand cells. The representation of the computational mesh, both volume and surface meshes, can be found in Figure 2.

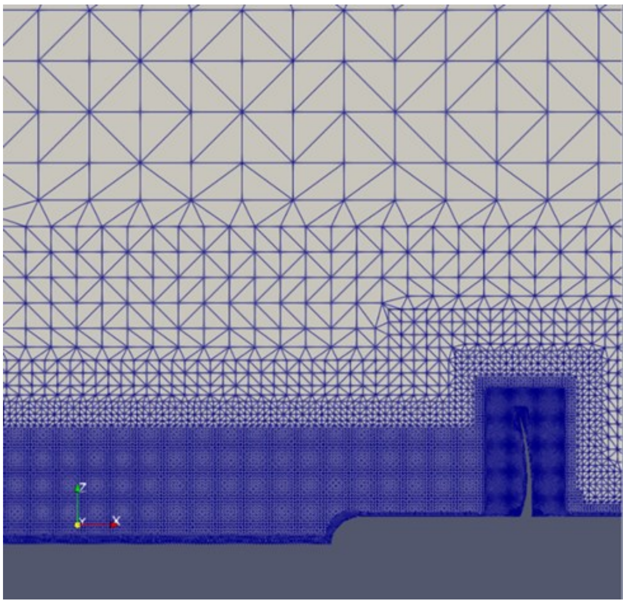

Slice of volume upwind of the blade.

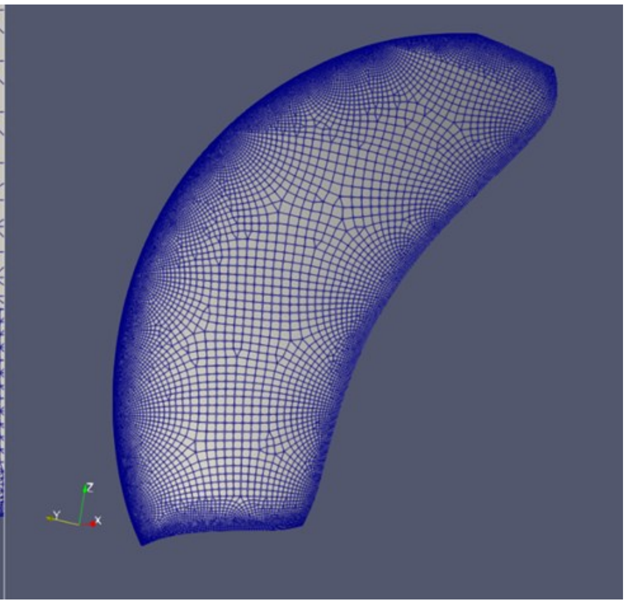

Surface mesh of the blade.

Figure 2: Mesh visualization.

Since the simulations are considered to reach a steady state, solving at the rotational (body-fitted) frame of reference is natural. We choose a constant rotational speed of $\omega = -9.46\, rad/sec$ and a varying inflow speed consistent with the target advance coefficient. Simulations are run for advance coefficient values of $J = 0.3, 0.4, \dots, 0.8$ with step of 0.1.

3.4 Results for the air-water stream cases

The open water characteristics of the propeller with the presence of a mixture jet can be found in **Errore. L'origine riferimento non è stata trovata.**. Three air/water mixture cases for the jet are tested, which consist of 90%, 95% and 100% water, respectively. In the 100% case, this is a pure water mixture.

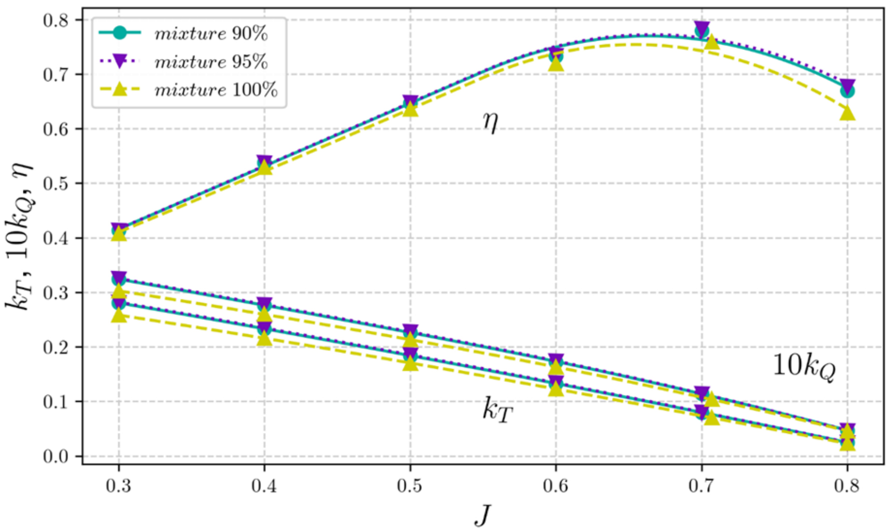

Figure 3: Blade thrust coefficient, torque coefficient and the efficiency grade over the advance coefficient.

It can be seen that compared to the single-phase performance, there is a slight increase in efficiency when a mixture jet is present. This is valid for a mixture of 90% as well as for a mixture of 95%. There is a slight increase in efficiency for all advance coefficients, while the maximum efficiency gain is noted for J=0.7 and J=0.8. The increase in performance can be attributed to the direct effect of the dynamic viscosity of the mixture on the drag force of the propeller blade. This means that, significantly lower dynamic viscosity (in the stream region) results in smaller drag contributions to the entire propeller blade when the jet is present. Finally, in Figure 4 density and pressure contours of the flow around the propeller can be found. We can easily distinguish the jet region, which, closer to the blade, starts to shrink its span and diverge from its initial centre line. This results from the jet's interaction with the rotating propeller blade, where flow is accelerated. Also, the propeller's wake is visible when the shape of the air-water jet is observed right at the aft of the blade.

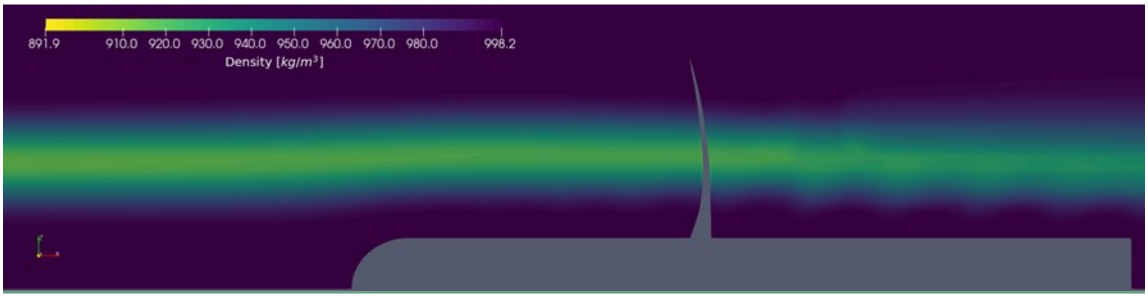

Density contour plot of a XZ slice.

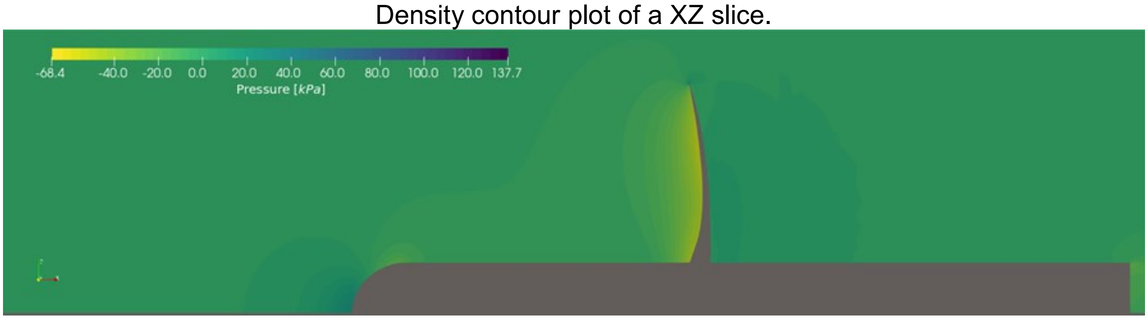

Pressure contour plot of XZ slice.

Figure 4: RETROFIT55 propeller density and pressure visualizations using mixed inlet at J = 0.7.

4 Injection through a slit with the use of a plate

The second approach differs in set-up and in how the air-water mixture is introduced into the propeller plane. Rather than the air being introduced as a jet, a plate with a slit is used to introduce the air-water mixture. This representation more closely correlates to how air would be injected in reality. By using a slit in a plate, the quantities of air and water can be varied as required. After passing through a short, recess (the slit), the air-water mixture is introduced to the global flow of water in the domain. The global flow of water in the domain then meets with the air-water mixture and carries the mixture towards the propeller, which is downstream of the injection point. A representation of the geometric set-up is shown in Figure 5**Errore. L'origine riferimento non è stata trovata.**. The slit is located 2.485 m from the downstream edge of the plate, and this edge is aligned with the tip (or nose) of the propeller hub.

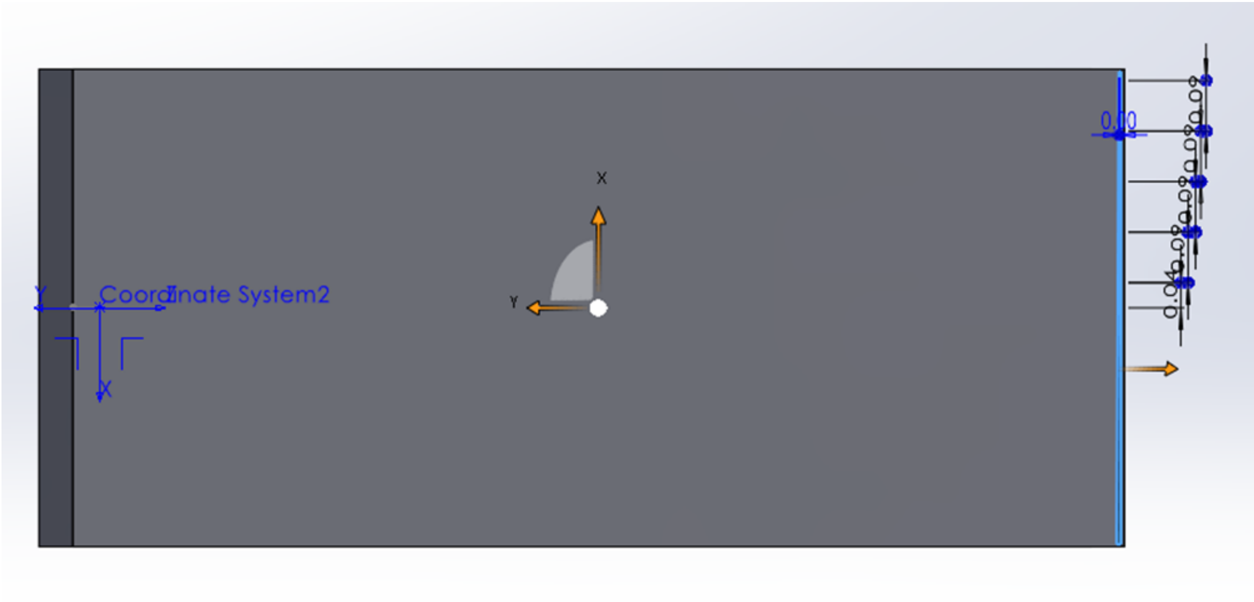

Figure 5: Plate geometry showing the location of the tapered slit.

he slit is slightly tapered to introduce an element of perturbation to the flow and, to an extent, direct it towards the propeller working area; without this taper, the air-water mixture travelled along the plate in a linearised way but tended to dissipate before forming an air layer or reaching the propeller. The introduction of the taper combated these tendencies and allowed for a partial air layer to form. In model and full-scale testing, the air is introduced via injectors rather than a continuous slit. So, it was desirable to decrease the level of linearisation in the flow.

The propeller geometry takes the same form as in the first approach and is included at the opposite end of the plate from the injector slit. The propeller is a 5-blade propeller. The propeller and plate are scaled down 1:56 from the full-scale versions. The plate represents the Japanese Bulk Carrier (JBC) geometry, which has a maximum beam at the waterline of 45.0 meters, meaning in the simulation's scaled version, the plate's width was 0.804 meters.

4.1 CFD simulation details

The approach for the second work set used the commercial CFD package STAR CCM+, with the simulations being run on LJMU's in-house HPC facility, PROSPERO [12]. In this work, an implicit unsteady approach was utilised due to the unsteady nature of the phenomena. For temporal discretisation, the simulation uses an implicit unsteady approach for a coupled flow and a 1st-order temporal discretisation scheme. The modelling approach used was the VOF modelling approach, which was used in a single-phase and a multi-phase manner. Researchers have used the VOF approach to multiphasic modelling in replicating a significant range of flow topographies, including slug flow and stratified layers [13]. The VOF Approach to fluid flow modelling is a prominent approach to handling multiphasic simulation; however, it does not allow for the phases to be interpenetrating, representing the phases as having a distinct boundary [14]. It is acknowledged that due to the agitative and mixing effect of the propeller, the assumption of immiscible fluids in the VOF approach limits the replication level that can be achieved using this method. Still, using this model allows for some of the effects of air ingress to be modelled and the assessment of the thrust and torque effects. To consider the interpenetrating nature of the two phases, alternative modelling, such as Eulerian multiphase modelling, would need to be considered, and future work should look towards alternative modelling approaches.

The chosen turbulence model remained in line with the first approach and utilised the $k - \omega\, SST$ turbulence model. This turbulence modelling approach was utilised as opposed to the $k - \varepsilon$ model for several reasons, primarily due to the significance of the near-wall characteristics and the desire for the turbulence modelling approach to best represent these characteristics. Secondarily, it was noted that there was a good level of precedent regarding the use of the $k - \omega\, SST$ model in the simulation of air lubrication. The primary water phase was modelled as an incompressible fluid, and the secondary air phase was modelled as a compressible gas.

The propeller's rotation is modelled using a rotating region/mesh approach. The rotating mesh region encompasses the propeller geometry and has a rotational rate imparted upon it. As discussed above in section 4, the propeller and plate geometry are a 1:56 representation of the full-scale geometry; therefore, the propeller's rotation was scaled using Froude scaling.

The full-scale propeller rotation rate is $n_{fs} = 90\ RPM$. The scaled propeller's rotation rate n_{ms} can be computed as:

$$n_{ms} = \sqrt{\lambda} n_{fs}$$

where n_{fs} is the full-scale rotation rate and $\lambda$is the scale factor. Being $\lambda = 56$ then $n_{ms} = 673.5\ RPM$.

Due to the importance of the near wall and viscous sub-layer effects in the simulation, it was desirable to produce a y+ (non-dimensionalised wall distance) value below a value of 1, which was targeted in the mesh approach explained in the following section. In line with this y+ value, the $k - \omega$ wall distance option was targeted towards the low y+ wall distance option. However, the all y+ option was selected as with this choice where the y+ value is sufficiently low, it would behave as the low y+ wall distance option, and in the event the y+ value increases, this will ensure correct wall treatment.

4.2 Domain and meshing

The domain created was ‘bullet-shaped’, in line with other propeller and aerofoil simulations, which were considered [15, 16], as well as prior propeller CFD work carried out at LJMU. The domain was 7.85 meters in length and 2 meters in diameter. The curved face of the domain has a radius of 1m. The domain size meets and exceeds ITTC recommendations on the domain size for CFD testing [17, 18]. A representation of the domain is shown in Figure 6.

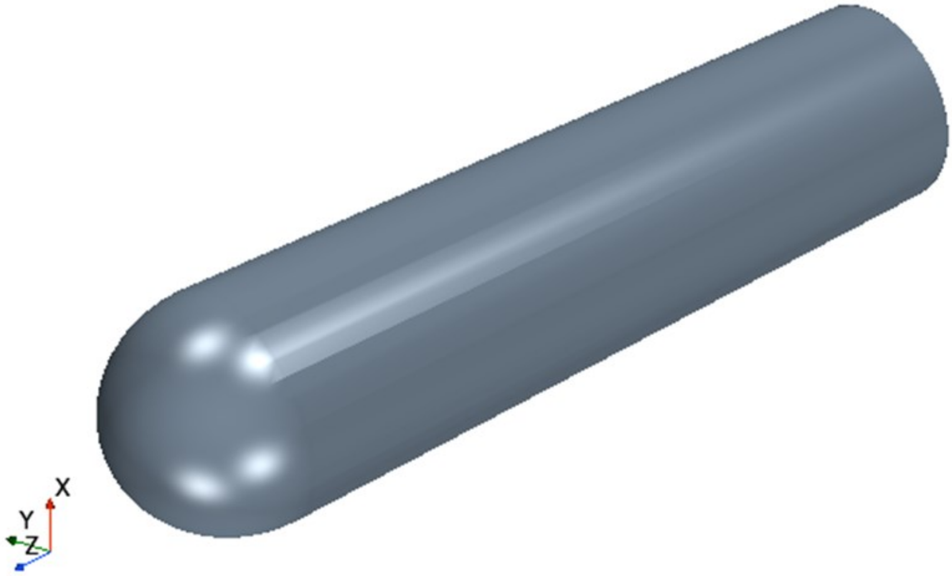

Figure 6: Representation of the ‘bullet-shaped’ domain.

The curved face of the domain is specified as a velocity inlet, where the inflow velocity is varied from 0.894 m/s to 1.169 m/s in line with the CNR towing tank test velocities indicated at the time of this work. The end of the domain face is specified as a constant pressure outlet, and the corresponding phase field function specifies outlet volume fractions. The remaining faces are specified as no-slip wall boundaries.

The rotating region in relation to the plate is shown in Figure 7, this gives a small propeller blade tip clearance from the plate and ensures that the introduced air-water mixture will travel into the propeller plane. It is important to note that including the propeller and rotating region in this way does not represent the propeller's real-world relation to the hull. It should be noted that variations in the air lubrication system used, the quantity of air introduced, and the hull geometry will affect the amount of air entrained within the propeller region. For example, the work carried out by a range of authors on alternative air lubrication systems indicated that air did not directly enter the propeller plane for the conditions and cases that they considered. However, they suggest that introducing air into the propeller can affect propulsive characteristics and reduce thrust and torque coefficients. Upon the boundary between the rotating and non-rotating regions, a phase-permeable interface boundary is specified where fluid from each region can pass to the other.

Figure 7: Rotating region in relation to the plate.

The chosen meshing approach used for both the rotating and non-rotating regions was a trimmed-cell mesh, and prism layers were used in the rotating region to ensure capture of the near-wall effects and accurate prediction of the propeller propulsive characteristics. The use of polyhedral meshing was also considered for the work, mainly to investigate the best representation of the propeller geometry. On the propeller geometry, a series of surface refinements were set. These were on the nose, propeller blade root, face, and at the blade edges/tips. The additional mesh refinement across the propeller was seen as imperative, both for the correct representation of the propeller and for accurate prediction of the propulsive characteristics. A representation of the mesh around the propeller is seen in Figure 8. Extracting the y^+ value after processing the simulation data will confirm the desired y^+ value.

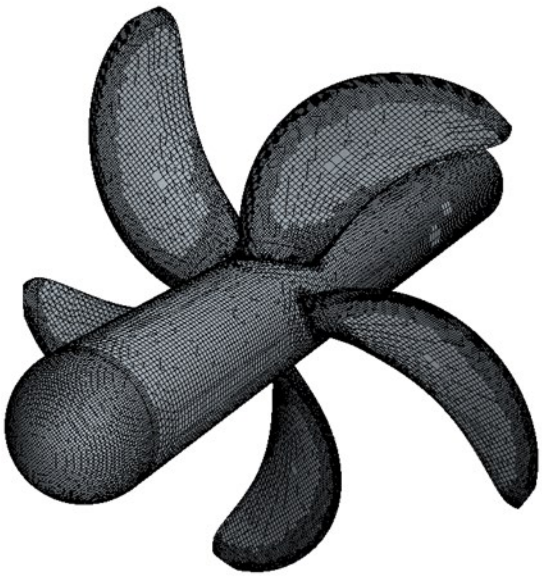

Figure 8: Representation of the mesh around the propeller.

Although less imperative for the simulation accuracy, the mesh on the plate and the slit were also refined, as this will contribute to the representation of the air layer as it travels across the plate and into the propeller plane. This created a very dense mesh on the underside of the plate, with a view that this would produce a good representation of the air layer distribution and topography on the underside of the plate.

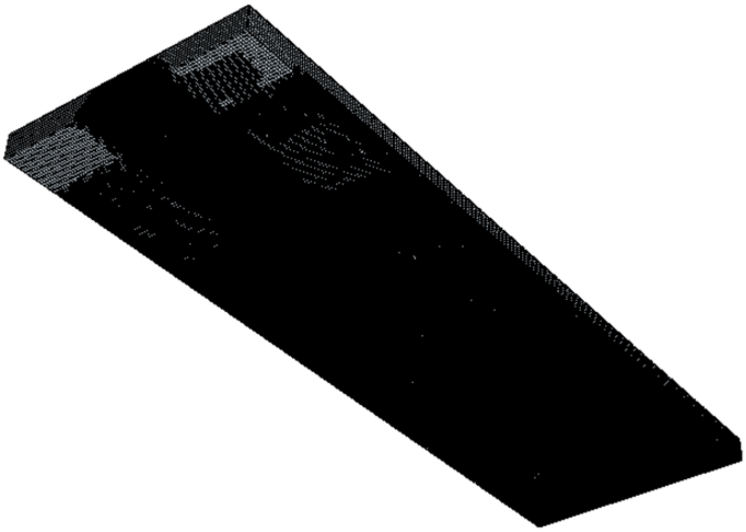

Figure 9: Underside of the plate mesh.

A representation of the mesh on the underside of the plate is seen in Figure 9**Errore. L'origine riferimento non è stata trovata.**, and a representation of the top of the plate can be seen in Figure 10.

Figure 10: Top of the plate mesh.

4.3 Single-phase simulation baseline

Although existing propulsive data is available for the propeller form used in this work, the presence of the plate in this simulation means that the generated thrust and torque coefficient values do not correspond with the open-water data available.

For this reason, it was necessary to carry out single-phase propeller simulations at the desired global velocities. Creating these single-phase cases allows for comparing the multi-phase results with the single-phase results, and the impact of the introduction of air to be considered in isolation from any impact from the geometry. The results for the baseline are shown in Table 1.

Table 1: Baseline propeller thrust and torque data.

Inflow velocity [m/s]	Thrust coefficient	Torque coefficient	Kt/10*Kq
0.894	0.150	0.317	0.474
0.997	0.135	0.300	0.449
1.066	0.141	0.310	0.457
1.169	0.172	0.353	0.487

Typically, with propeller simulations, the operator considers the open-water velocity when calculating the advance coefficient for the propeller. However, it is important to note that in this work, the range of inflow velocities is relatively limited, with a range of 0.275 m/s between the lowest and highest velocities. The presence of the plate caused a reduction in the perceived inflow velocity to the propeller, and this explains why the thrust and torque coefficients saw this behaviour, as in some cases, the perceived inflow velocity was higher and, in some cases, lower. In any case, as these results represent comparative data for the multi-phase results, they are suitable for considering the impact of air ingress on the propeller. Furthermore, rather than considering the propeller efficiency, the ratio of thrust coefficient to 10*torque coefficient indicates how torque is transferred into thrust. It is accepted that the use of Kt/10Kq is a limited comparison, and it would be preferable to use propeller efficiency; however, due to the variation in propeller inflow velocity mentioned, it was accepted that this limited comparative element would be used to demonstrate the change in thrust coefficient relative to torque coefficient.

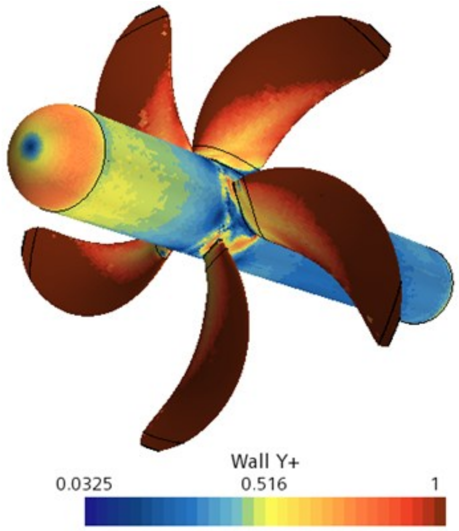

Figure 11: Plot of the y+ value on the propeller.

Acknowledging the focus and limitations of this work, future investigations should further consider the under-plate velocity profile and modified inflow velocity to the propeller, either by alternative modelling approaches or experimental testing.

From the single-phase results, it was possible now to assess the y+ value on the propeller geometry, and this confirmed that the y+ value across the geometry remained below the desired value of 1. A plot of the y+ value on the propeller is shown in **Errore. L'origine riferimento non è stata trovata.**.

4.4 Multi-phase results

For the multi-phase simulation, the air-water mixture was introduced to the domain via a slit in the plate. With this in mind, there was one adjustment made to the simulation set-up, which was that the plate slit was specified as a mass flow inlet. The simulation cases for the multi-phase work were divided into three sets of air-water injection cases, with an additional data set considered, which is supplementary, where air is injected exclusively. The first simulations were conducted under the CNR ‘as designed’ conditions for the towing tank testing. The second set of simulations was created by varying the air injection rate while keeping the water injection rate constant. The third set of simulations was created by varying both the injection rate of air and water. In the supplementary cases, air was injected through the slit exclusively.

4.5 As designed multi-phase cases

The first simulation set corresponded to the conditions designed by CNR for the JBC model in physical testing. This was an airflow rate of 0.00242 m^3/hr per inlet and a water inflow rate of 0.01278 m^3/hr per inlet. Converting this to a corresponding mass flow rate for the air and water gives a mass flow rate of air of $7.90945 \cdot 10^{-7}$ kg/s per inlet and a mass flow rate of water of $3.54134 \cdot 10^{-3}$ kg/s per inlet. Therefore, the combined mass flow rate is $3.54213 \cdot 10^{-3}$ kg/s per inlet.

The mass fraction for both was determined to introduce the required quantity of air and water; for the as-designed cases, this was a mass fraction of 0.000223296 for the air and 0.999776704 for the water. Finally, this gave a volume fraction for the air of 0.159210526 and the water of 0.840789474.

A 14-inlet set-up for the plate was used. Therefore, the total mass flow rate for the slit was $4.95898 \cdot 10^{-2}$ kg/s. The approach to introducing this air was to specify the total mass flow rate of the combined air and water on the inlet and specify the corresponding volume fractions. For the as-designed cases, the results showing the change in thrust and torque coefficient, as well as Kt/10Kq are reported in Table 2 and graphically in Figure 12.

Table 2: 'As designed' condition results.

Inflow velocity (m/s)	% Change in thrust coefficient	% Change in torque coefficient	% Change in Kt/10Kq
0.894	-1.578	-1.570	-0.008
0.997	-0.055	-0.436	0.383
1.066	0.097	-0.498	0.598
1.169	-1.587	-1.593	0.006

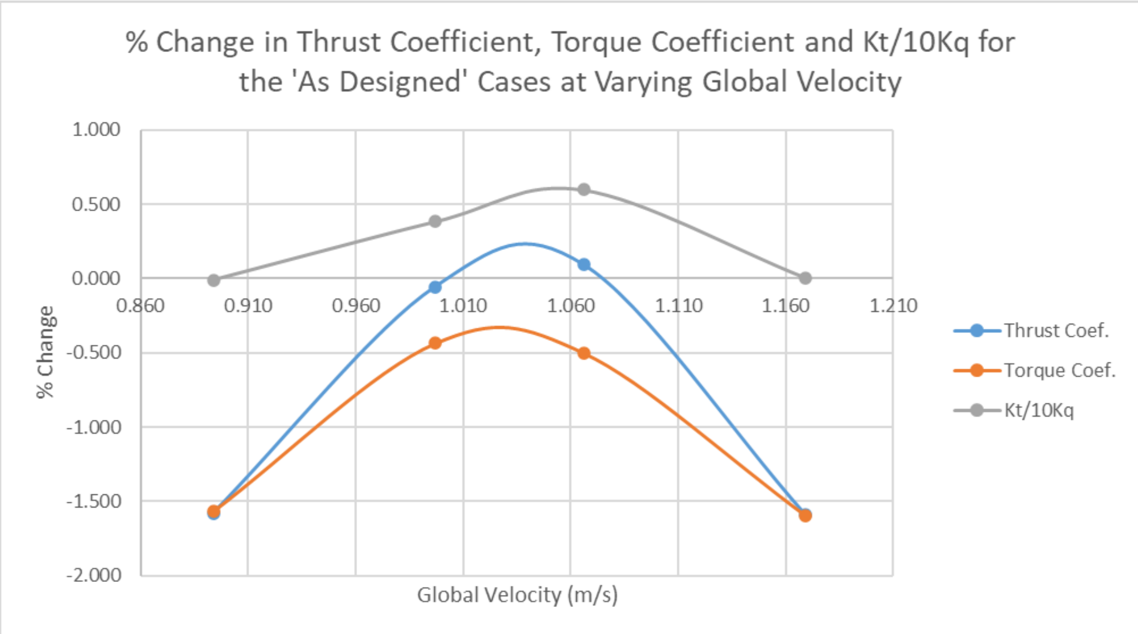

Figure 12: Thrust coefficient, torque coefficient, and Kt/10Kq for the 'As Designed' condition.

The results of the 'As Designed' condition tests indicate that introducing air into the propeller has resulted in a slight decrease in thrust and torque coefficient of around 1.5% at the lowest and highest velocities. In the two intermediate velocities, the thrust and torque coefficient were less impacted by the air ingress, with the torque coefficient decreasing slightly (around 0.5%) and the thrust coefficient remaining close to unchanged. It is suspected that in the 'As Designed' condition, the quantity of air reaching the propeller was limited, and this was confirmed by the scene produced in Figure 13. The air constrained below the plate remains at a very low volume fraction for the cases considered and so in addition to Figure 13, additional higher contrast images were produced in Figure 14 and Figure 15.

Figure 13: Volume fraction of air scene for the 'As Designed' condition (0.997 m/s case).

Higher contrast images of the scene are shown in Figure 14 and Figure 15, demonstrating the ingress of air into the propeller despite the low volume fraction. Similarly, a scene of the volume fraction of air on the propeller surface was produced, as shown in Figure 16. Once again, the volume fraction indicates that the quantity of air at the propeller surface, the 'effective' air, is minimal.

Figure 14: High contrast image 1 for the 'As Designed' condition (0.997 m/s case).

Figure 15: High contrast image 2 for the ‘As Designed’ condition (0.997 m/s case).

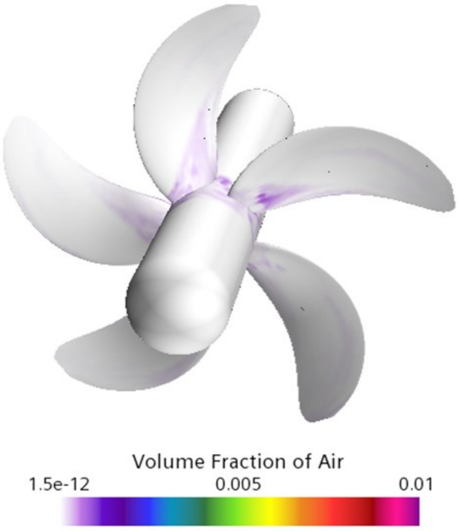

Figure 16: Volume fraction of air on the propeller geometry for the ‘As Designed’ condition (0.997 m/s case).

As the 0.997 m/s case showed minimal change in thrust and torque coefficient, the same scene was produced for the 1.169 m/s case, which showed the most significant change in thrust and torque coefficient, to assess any notable differences. The corresponding images for the 1.169 m/s cases are shown in Figure 17 to Figure 20.

Figure 17: Volume fraction of air scene for the ‘As Designed’ condition (1.169 m/s case).

Figure 18: High contrast image 1 for the ‘As Designed’ condition (1.169 m/s case).

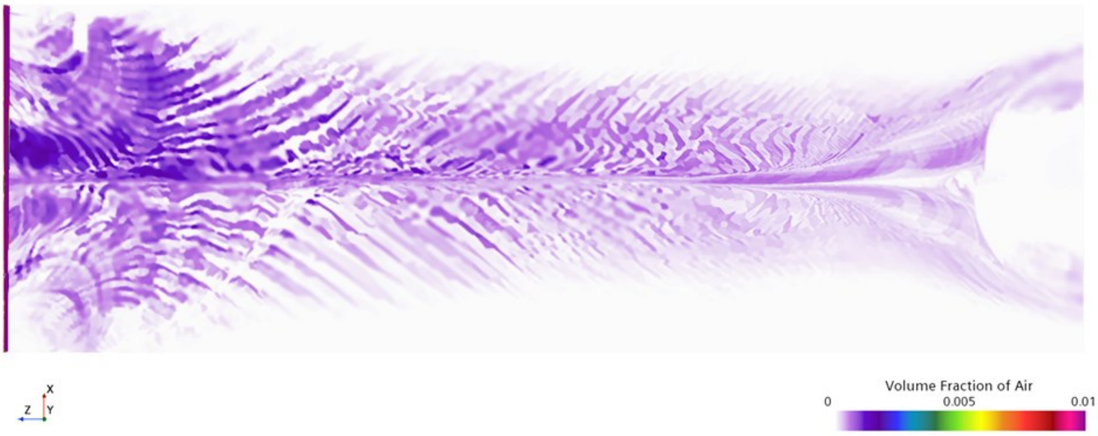

Figure 19: High contrast image 2 for the ‘As Designed’ condition (1.169 m/s case).

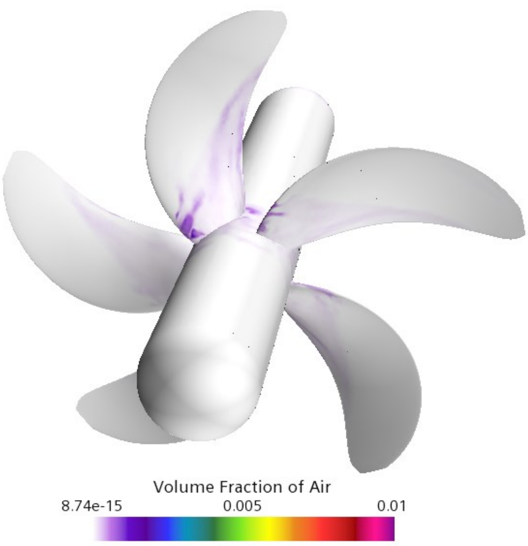

Figure 20: Volume fraction of air on the propeller geometry for the 'As Designed' condition (1.169 m/s case).

The comparison of the 0.997 and 1.169 cases would not indicate a significant difference in air distribution or entrainment in the propeller. The air carpet in the 1.169 m/s case is somewhat more established than in the 0.997 m/s case. It also appears that the propeller may have more air entrainment in the 1.169 case, specifically in the 3rd quarter of the blade face (as viewed from hub to tip).

The air distribution and ingress in the propeller for this work have been assessed in the manner described here. However, it would be pertinent to extend this assessment further to quantify the air distribution to a greater extent, in future work.

4.6 Increased air cases

To further assess the impact of air ingress, the next set of simulation cases was produced by increasing the quantity of air injected in the air-water mixture whilst keeping the quantity of air the same. The air was increased in 50% increments, and the volumetric flow rates for each of the cases produced are shown in Table 3.

Table 3: Increased air cases.

Case Number	Water [m^3/hr]	Air [m^3/hr]	Air multiplier	Air/Water Ratio	Total volumetric flow rate [m^3/hr]
As Designed	0.012780	0.002420	1	0.189358	0.015200
1	0.012780	0.003630	1.5	0.284038	0.016410
2	0.012780	0.004840	2	0.378717	0.017620
3	0.012780	0.006050	2.5	0.473396	0.018830
4	0.012780	0.007260	3	0.568075	0.020040
5	0.012780	0.008470	3.5	0.662754	0.021250
6	0.012780	0.009680	4	0.757433	0.022460

The data shown in Table 3 is for each outlet and is input to STAR CCM+ as a total combined mass flow rate for the 14 injectors with corresponding volume fractions via the same method as described in section 4.5. These values are shown in Table 4.

Table 4: Volume fractions and combined mass flow rates for the increased air cases.

Case Number	Volume fraction air	Volume fraction water	Star CCM combined mass flow rate [kg/s]
As Designed	0.159211	0.840789	0.049590
1	0.221207	0.778793	0.049595
2	0.274688	0.725312	0.049601
3	0.321296	0.678704	0.049606
4	0.362275	0.637725	0.049612
5	0.398588	0.601412	0.049618
6	0.430988	0.569012	0.049623

Cases 1 to 6 were then run at the global velocities (0.894, 0.997, 1.066, 1.169 m/s) to assess the impact of increasing the air quantity in the air-water mixture on the propeller upon thrust coefficient, torque coefficient and Kt/10Kq. The results are shown in Figure 21 to Figure 24.

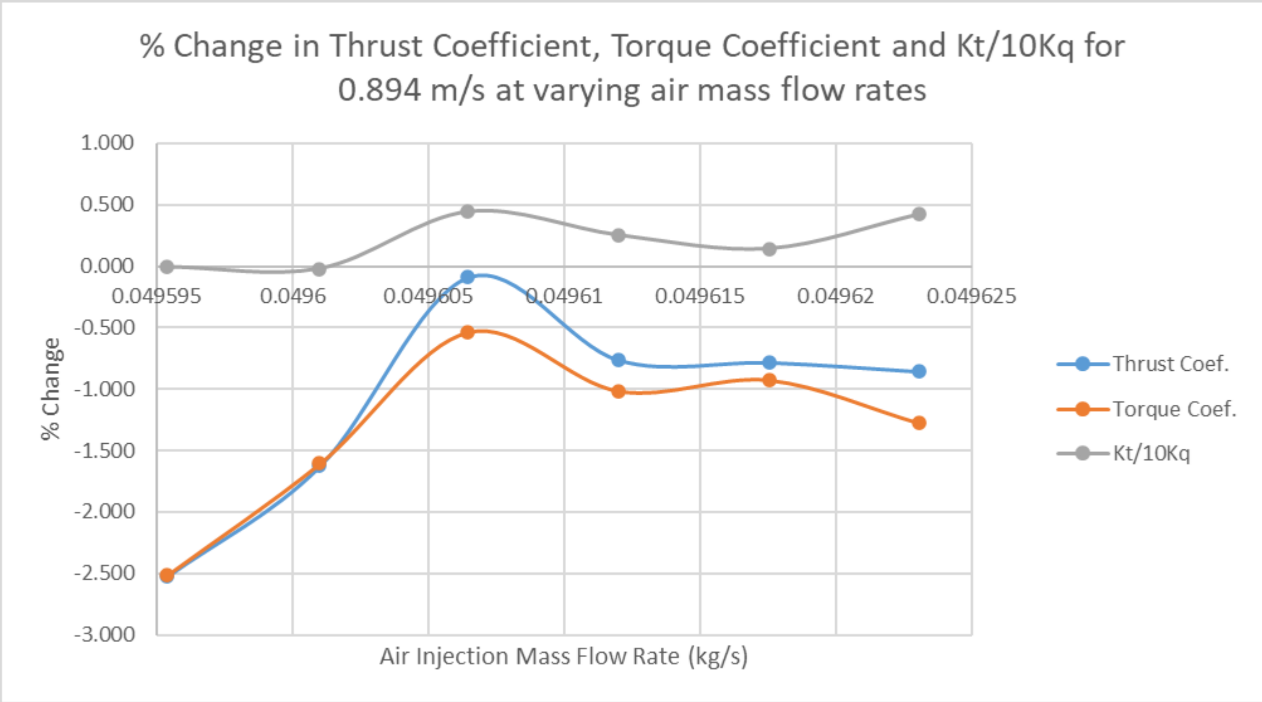

Figure 21: Increased air results for 0.894 m/s.

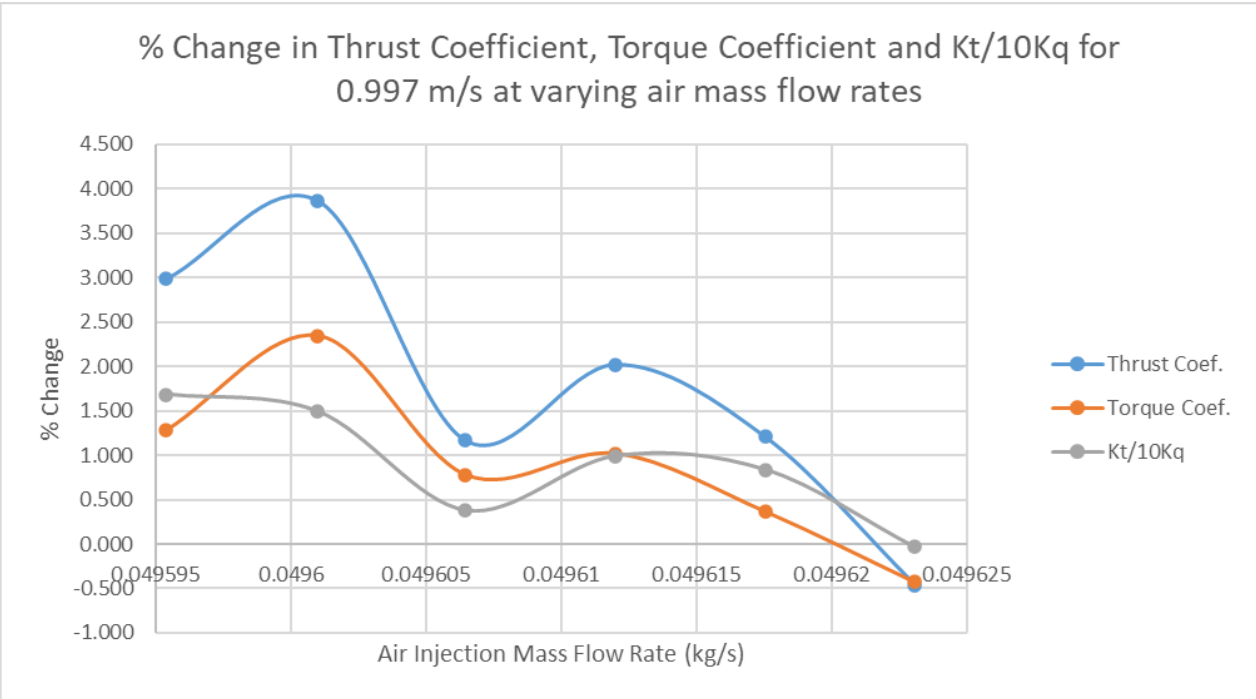

Figure 22: Increased air results for 0.997 m/s.

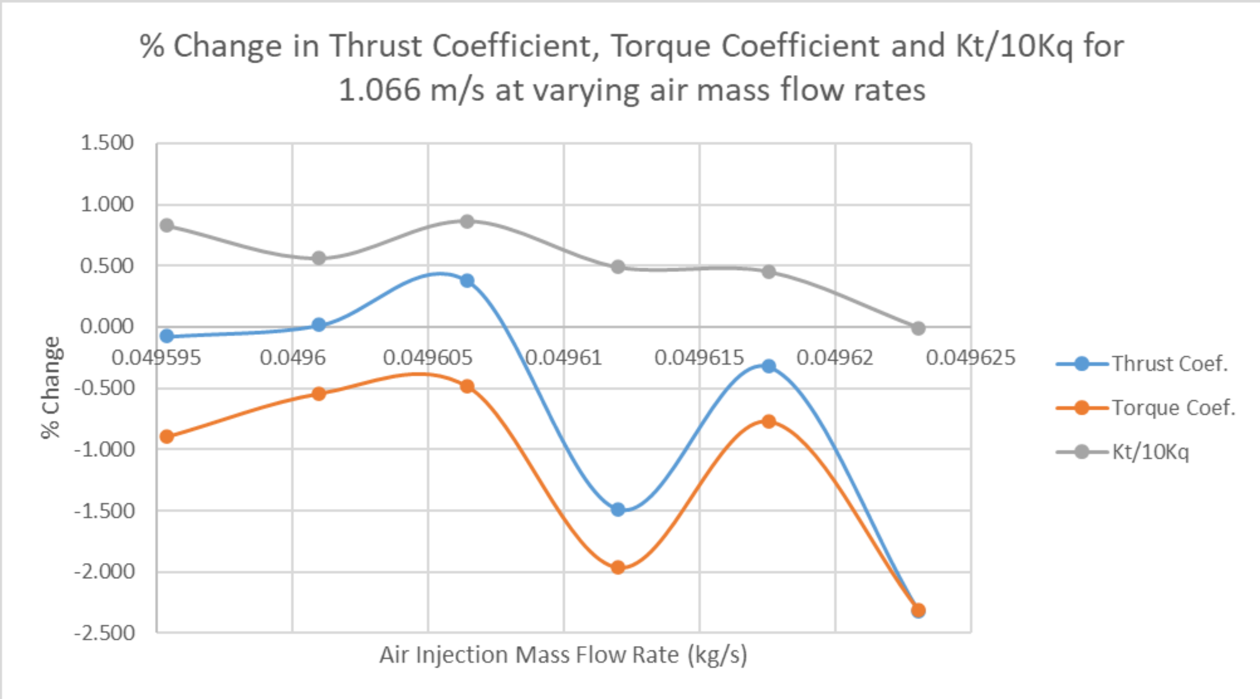

Figure 23: Increased air results for 1.066 m/s.

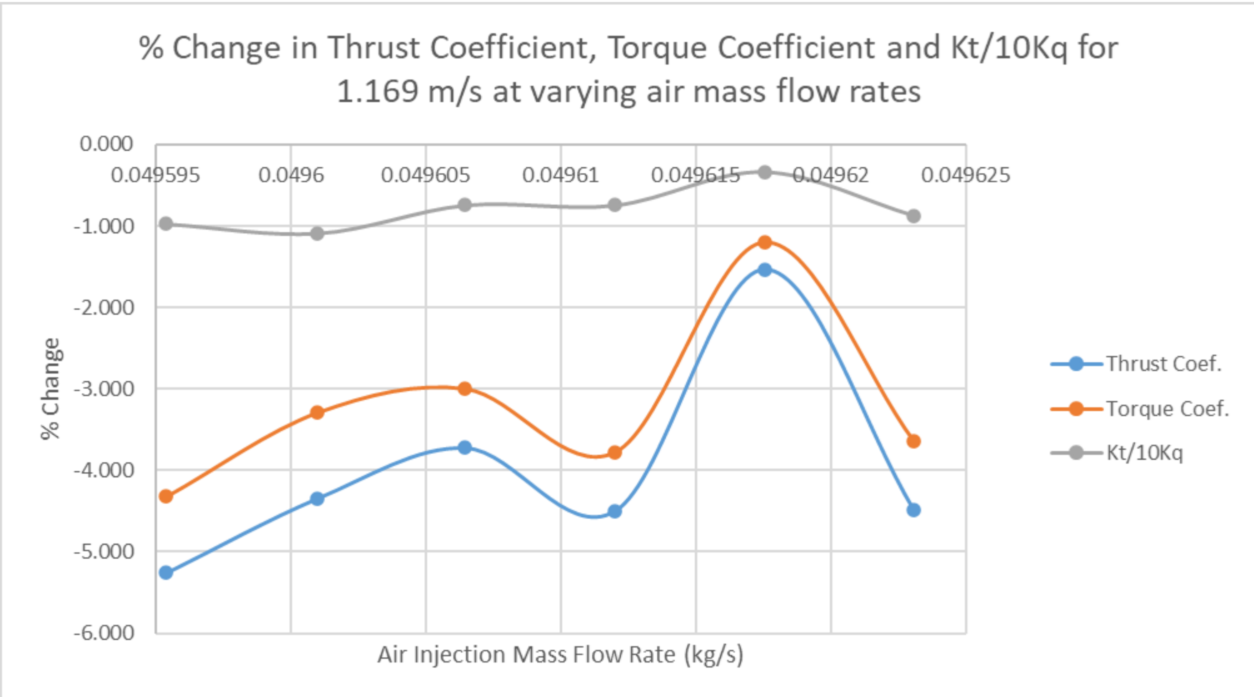

Figure 24: Increased air results for 1.169 m/s.

A thrust and torque coefficient reduction was seen in most cases for this simulation set. There is a notable exception to this in the 0.997 m/s cases, where an increase in thrust and torque coefficient was seen in most cases. If a reduction in thrust and torque coefficient is seen in the results, it was expected that, as the quantity of air is increased, this would lead to an increasingly detrimental effect, with assumed greater air ingress; however, these results indicate that the effect witnessed was not as straightforward as this. In the 0.894 and 1.169 m/s cases, the most significant thrust and torque coefficient reduction was seen at the lowest air injection rate. In contrast, in the 0.997 and 1.066 m/s cases, the higher air injection rate cases correspond to the most significant change in the thrust and torque coefficient.

For the 0.894 m/s cases, aside from the lowest air injection rates, the thrust and torque coefficient reduction seem relatively consistent as the air injection rate varies. In the 0.997 m/s cases, aside from the highest injection rate, an increase in thrust and torque coefficient was seen, which was extremely interesting to witness and would be an indicator that, in some scenarios, air ingress in the propeller may have a supplementary effect on propulsive characteristics. In the 1.066 m/s cases, at the lower air injection rates, the change in thrust coefficient is minimal with a slight decrease in torque coefficient; before, in the third injection rate set-up, a slight increase in thrust coefficient corresponds to a small decrease in torque coefficient. The remaining cases at 1.066 m/s showed a decrease in both coefficients, but the extent of this varied. Finally, in the 1.169 m/s cases, both coefficients are reduced. Initially, in the 1.169 m/s cases, as the air injection rate increases, the extent of the decrease in thrust and torque coefficient decreases before fluctuating at the higher air injection rates.

Regarding the Kt/10Kq indicator, which was plotted, in most cases (aside from 1.169 m/s), this value appeared to increase with air injection, which tentatively may initially suggest that less torque is required to deliver the corresponding thrust. However, as discussed, across the results, a reduction in thrust and torque coefficient was generally seen; therefore, the apparent increase in Kt/10Kq is somewhat deceptive.

To investigate the nature of the air underneath the plate and on the propeller in these cases Figure 25 to Figure 27 were produced, which was taken from the 0.997 m/s Case 2 set-up, which showed the greatest increase in thrust and torque coefficient.

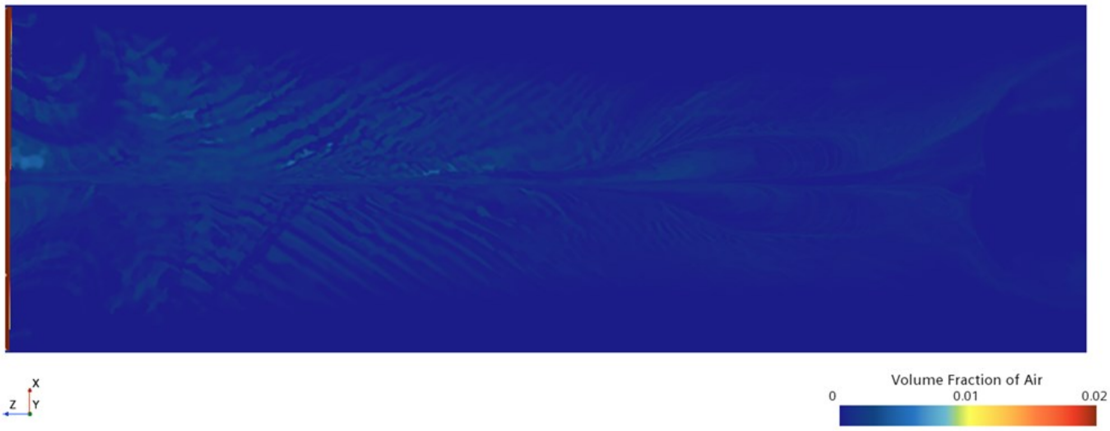

Figure 25: Volume fraction of air scene for the 0.997 m/s case 2 set-up.

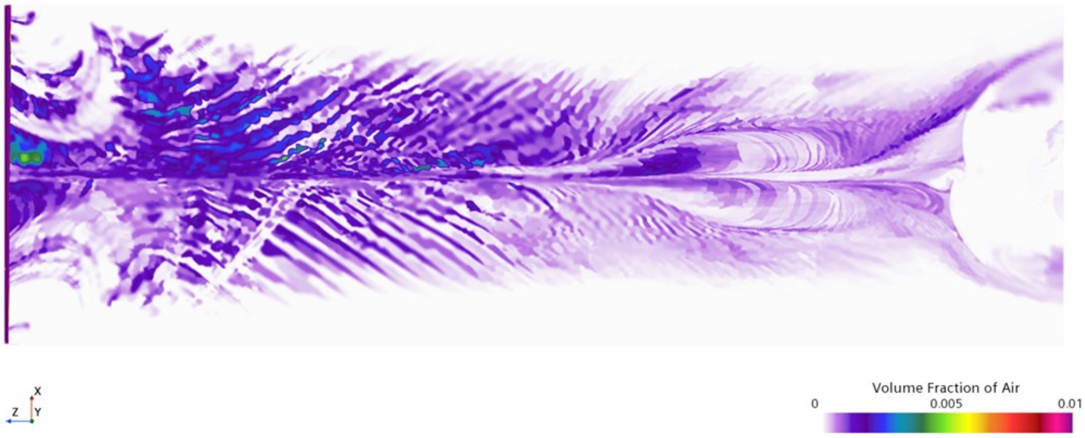

Figure 26: High contrast image for the 0.997 m/s case 2 set-up.

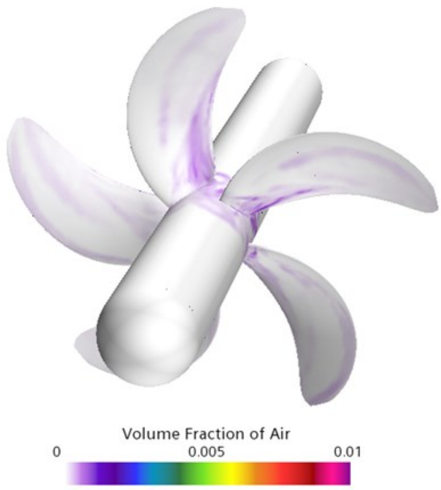

Figure 27: Volume fraction of air on the propeller geometry for the 0.997 m/s case 2 set-up.

Similarly, Figure 28 to Figure 30 were produced, corresponding to the 1.169 m/s case 1 set-up, which showed the most significant decrease in thrust and torque coefficient.

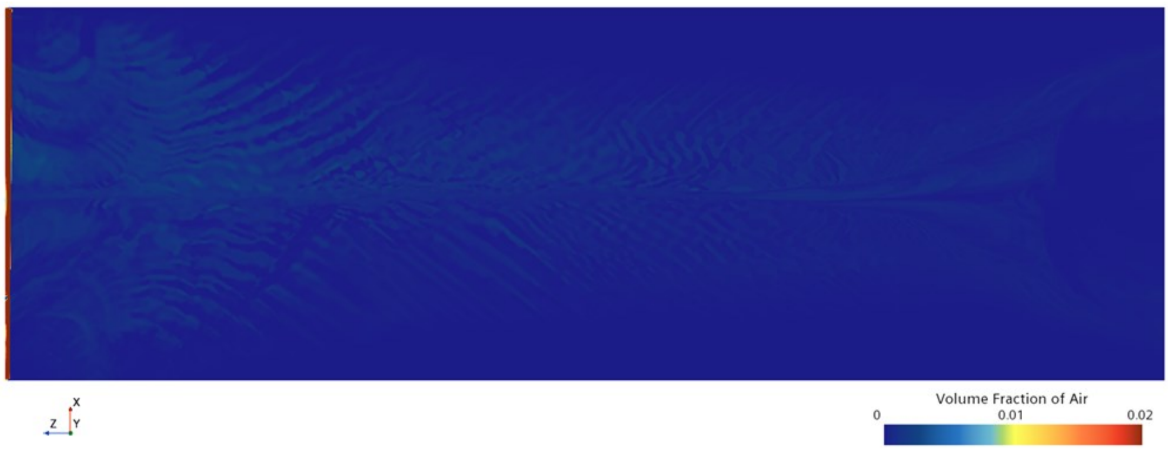

Figure 28: Volume fraction of air scene for the 1.169 m/s case 1 set-up.

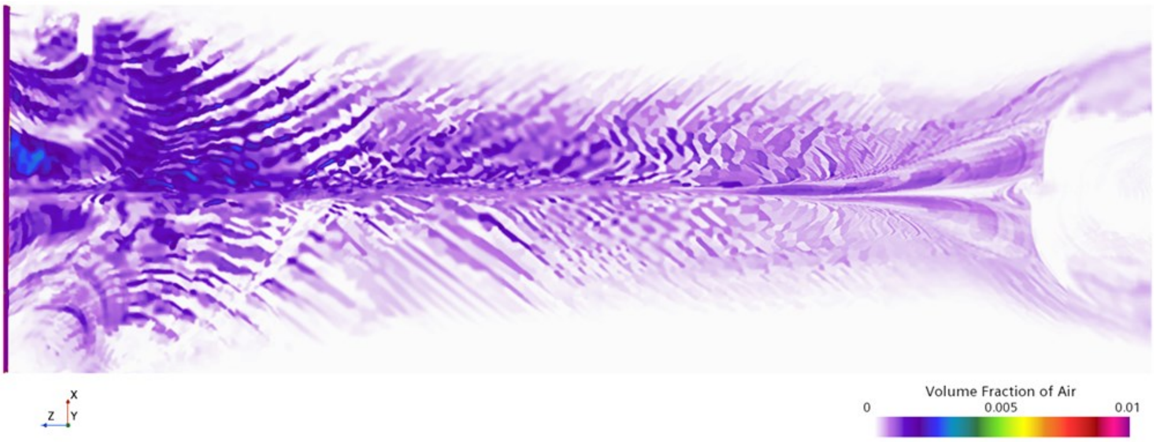

Figure 29: High contrast image for the 1.169 m/s case 1 set-up.

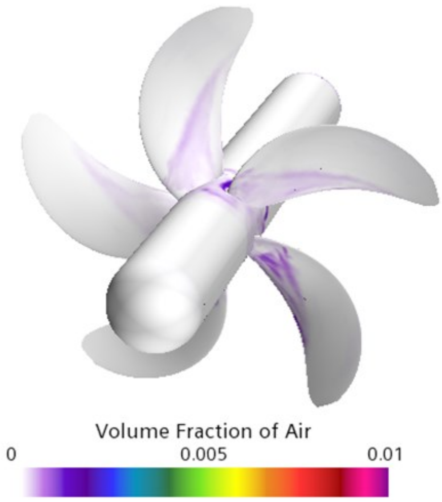

Figure 30: Volume fraction of air on the propeller geometry for the 1.169 m/s case 1 set-up.

Comparing the figures from the 0.997 m/s case 2 set-up and the 1.169 m/s case 1 set-up, there does not appear to be a considerable difference. The 0.997 m/s case shows a greater entrainment of air on the plate and the propeller due to the high-volume fraction areas seen on the plate and the darker regions indicated on the propeller. Comparison is limited to visual inspection in these cases, and it would be beneficial to investigate the air quantities further before conclusions are drawn.

The results of this simulation set suggest that air ingress into the propeller may have a detrimental effect on its performance. However, due to the somewhat irregular nature of the results obtained and, crucially, the beneficial results seen in the 0.997 m/s cases, it would not be appropriate to draw definitive conclusions based on these results alone. Instead, these results should be an indicative starting point for further research using experimental testing and other computational techniques which better resolve the interpenetrating nature of air and water than the immiscible assumption of the VOF model.

4.7 Increased air and water cases

In a similar manner to the increased air cases, the effect of increasing both the air and water inflow rates was investigated. The multiplier was applied to air and water flow rates from the as-designed case to produce cases 7 to 12. The air-to-water ratio remains the same because the multiplier is applied to both the air and water flow rates while the total flow rate increases.

Table 5: Increased air and water cases.

Case Number	Water [m^3/hr]	Air [m^3/hr]	Multiplier	Air/Water Ratio	Total Volumetric flow (m^3/hr)
As Designed	0.012780	0.002420	1	0.189358	0.015200
7	0.019170	0.003630	1.5	0.189358	0.022800
8	0.025560	0.004840	2	0.189358	0.030400
9	0.031950	0.006050	2.5	0.189358	0.038000
10	0.038340	0.007260	3	0.189358	0.045600
11	0.044730	0.008470	3.5	0.189358	0.053200
12	0.051120	0.009680	4	0.189358	0.060800

The data shown in Table 5 is for each outlet and is input to STAR CCM+ as a total combined mass flow rate for the 14 injectors with corresponding volume fractions via the same method as described in section 4.5. These values are shown in Table 6, once again, it is noted that the volume fraction remains the same for both the air and water due to the setup.

Table 6: Volume fractions and combined mass flow rates for the increased air cases.

Case number	Volume fraction air	Volume fraction water	Star CCM combined mass flow rate [kg/s]
As Designed	0.159211	0.840789	0.049590
7	0.159211	0.840789	0.074385
8	0.159211	0.840789	0.099180
9	0.159211	0.840789	0.123975
10	0.159211	0.840789	0.148770
11	0.159211	0.840789	0.173564
12	0.159211	0.840789	0.198359

Cases 7 to 12 were then running at the global velocities (0.894, 0.997, 1.066, 1.169 m/s) to assess the impact of increasing the quantity of air and water in the air-water mixture on the propeller upon thrust coefficient, torque coefficient and Kt/10Kq. The results are shown in Figure 31 to Figure 34.

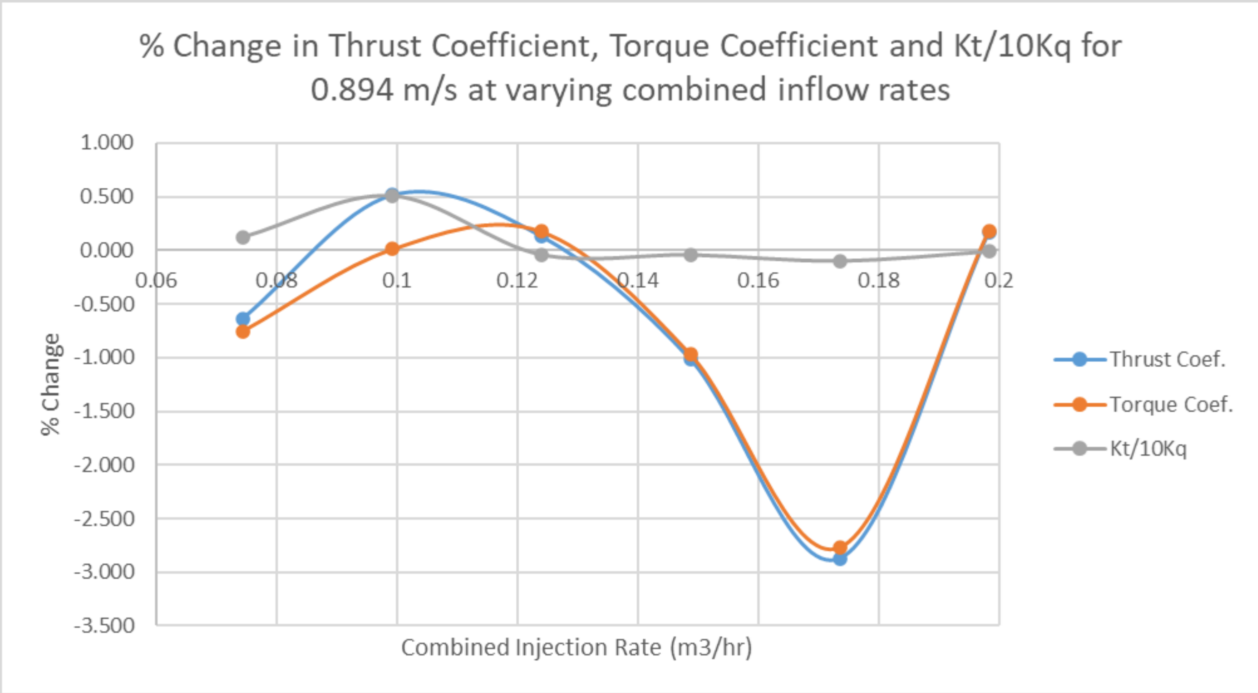

Figure 31: Increased air and water results for 0.894 m/s.

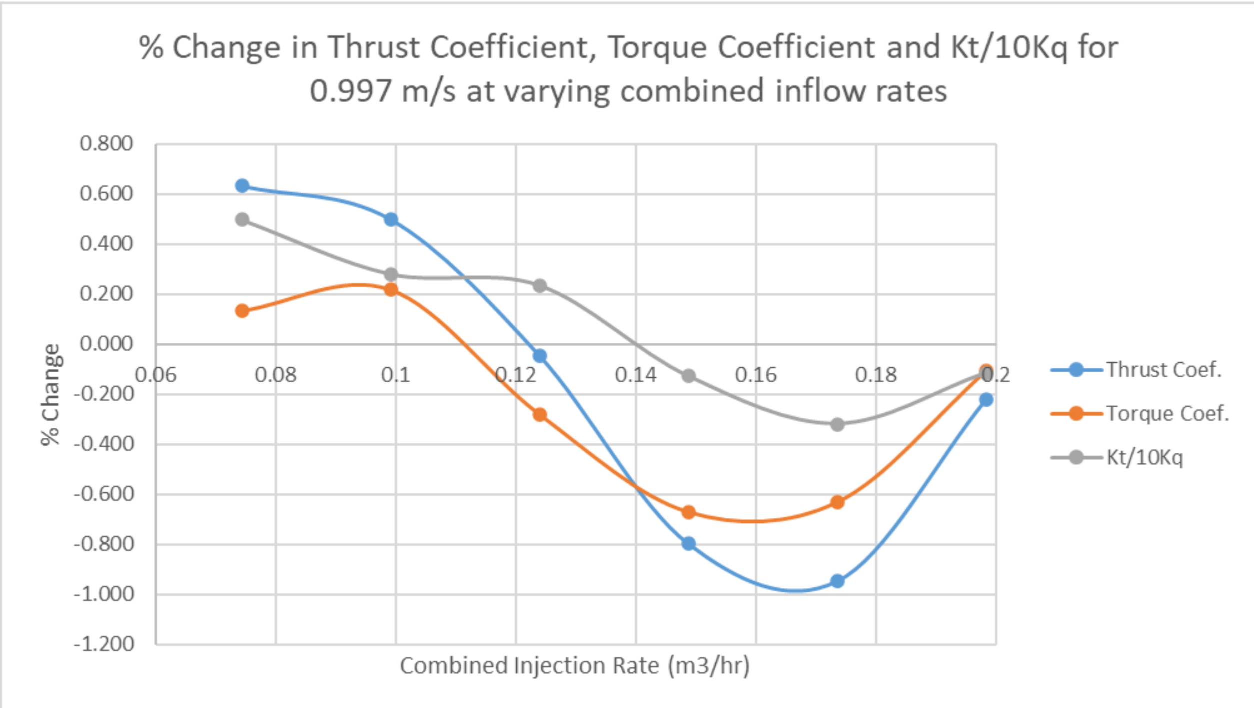

Figure 32: Increased air and water results for 0.997 m/s.

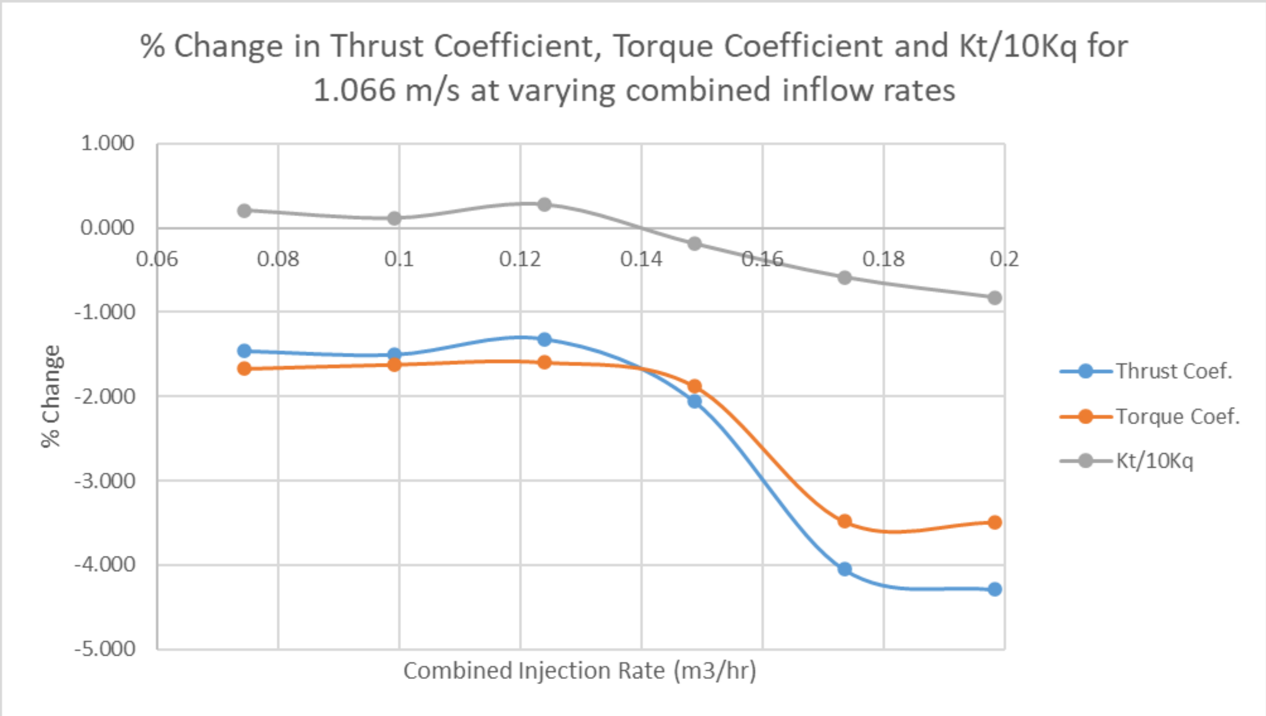

Figure 33: Increased air and water results for 1.066 m/s.

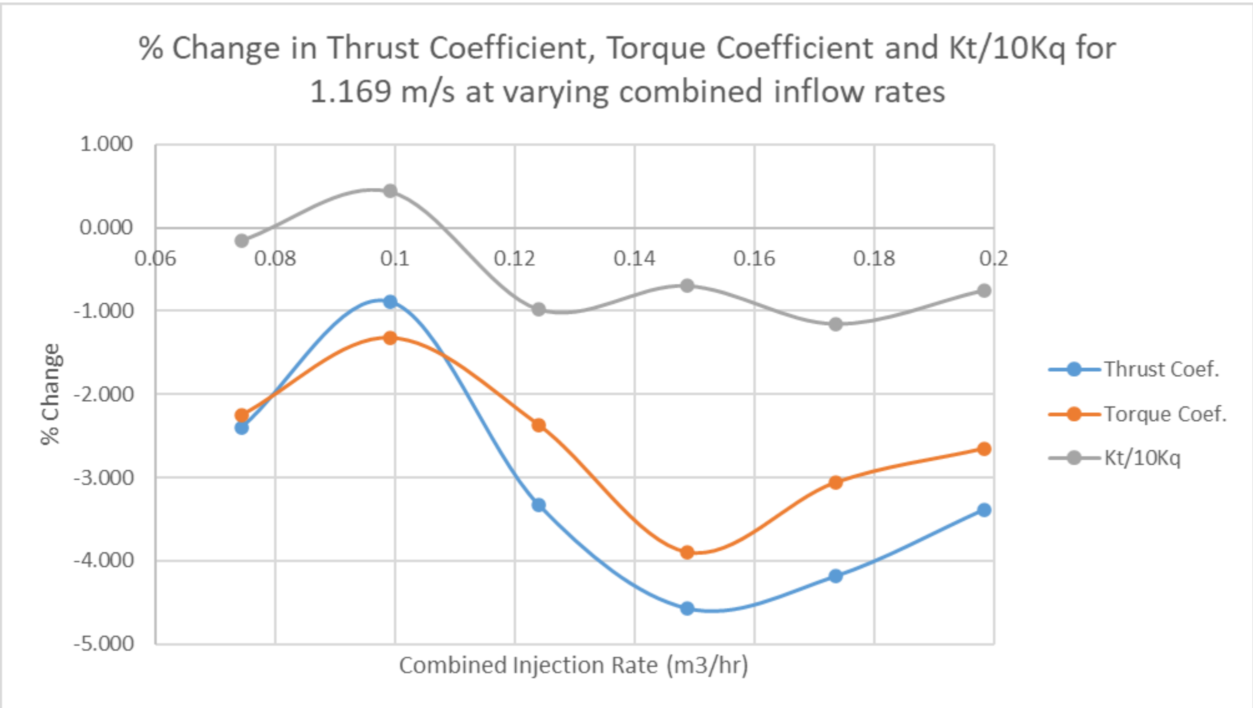

Figure 34: Increased air and water results for 1.169 m/s.

For most cases in this simulation set, a reduction in thrust and torque coefficient was seen, with notable exceptions in the 0.997 m/s cases and 0.894 m/s cases. In the 0.894 m/s cases, which did not show a reduction in the coefficients, the values remained close to unchanged or showed a small increase (around 0.5%). A notable result achieved from the 0.894 m/s cases, was for the case 12 set-up; as it appeared that the coefficients returned to being nearly unchanged from the baseline results. In the 0.997 m/s cases, at the lower injection rate cases, a slight increase in the coefficients was seen (around 0.6% or lower), and in those cases which did show a decrease in the coefficients, the decrease was below 1%. In the 1.066 m/s cases, the coefficient decrease was slight but relatively consistent between 1 to 2%, but in the highest injection cases, the coefficient decrease was larger. For the 1.169 m/s cases, the most significant reduction in thrust and torque coefficient occurred in the 1.169 m/s case 10 set-up, with the higher injection rates in case 11 and 12 set-ups showing a slight decrease in the magnitude of the reduction in thrust and torque coefficient.

What is perhaps most apparent when comparing the increased water and air cases to the earlier cases, which solely increased the air flow rate, is that when the air and water are increased together, more of the cases have shown a reduction in thrust and torque coefficient; however, it is not appropriate to draw conclusions on which set of simulation cases displayed the most significant reduction in thrust and torque coefficient due to the variability in the achieved results. In the air and water increased cases, the most significant reduction in thrust coefficient was around 4.5%. When the air was solely increased, a similar maximum decrease was seen of around 5%.

One behaviour seen exclusively in the cases where the air was solely increased is when the thrust coefficient increased by more than 1%, which should be investigated further to determine if this behaviour is an anomaly or an indicator of a broader behaviour. Regarding the Kt/10Kq indicator, which was plotted, a decrease in this indicator was seen in most cases. The reduction in Kt/10Kq values varied in the cases, with some showing a nearly unchanged value and others, such as in the 1.169 m/s cases, showing around a 1% reduction aside from the lowest injection cases. In the lowest injection rates for the 0.894 and 0.997 m/s cases, a slight increase was seen up to around 0.5%.

To investigate the nature of the air underneath the plate and the impact on the propeller in these cases, Figure 35 to Figure 37 were produced, which was taken from the 0.997 m/s Case 7 set-up, which showed the greatest increase in thrust and torque coefficient.

Figure 35: Volume fraction of air scene for the 0.997 m/s case 7 set-up.

Figure 36: High contrast image for the 0.997 m/s case 7 set-up.

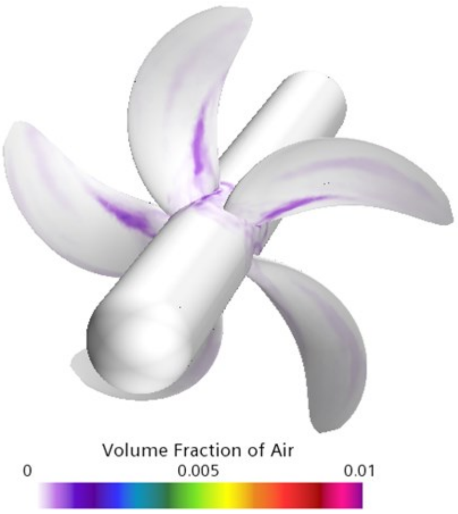

Figure 37: Volume fraction of air on the propeller geometry for the 0.997 m/s case 7 set-up.

Similarly, Figure 38 to Figure 40 were produced, corresponding to the 1.169 m/s case 10 set-up, which showed the most significant decrease in thrust and torque coefficient.

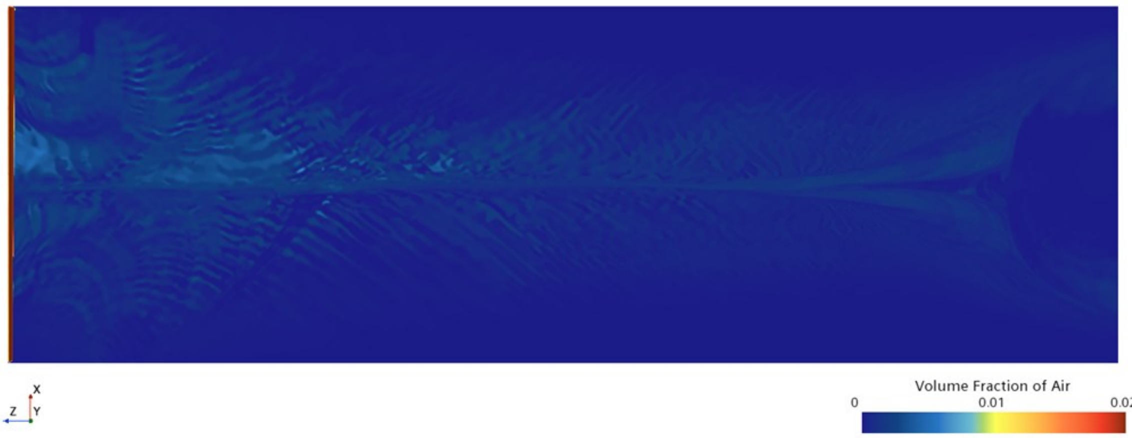

Figure 38: Volume fraction of air scene for the 1.169 m/s case 10 set-up.

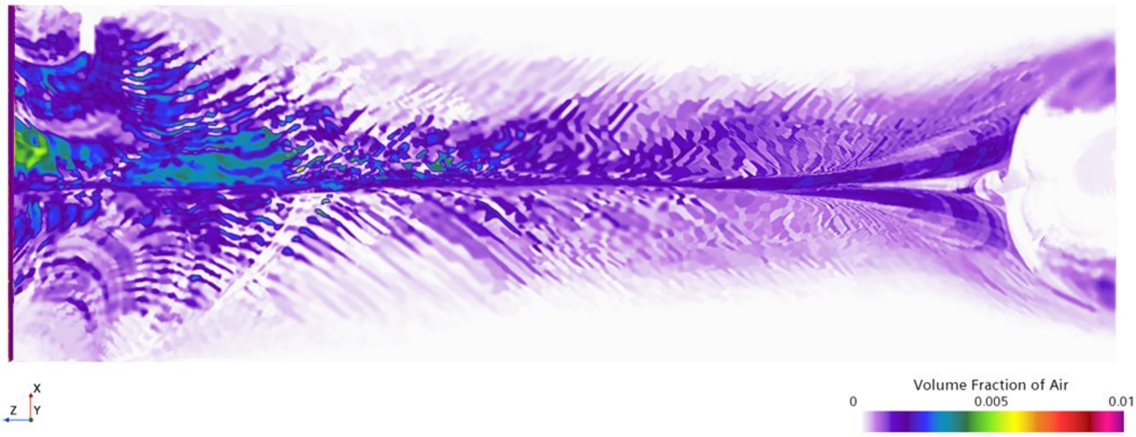

Figure 39: High contrast image for the 1.169 m/s case 10 set-up.

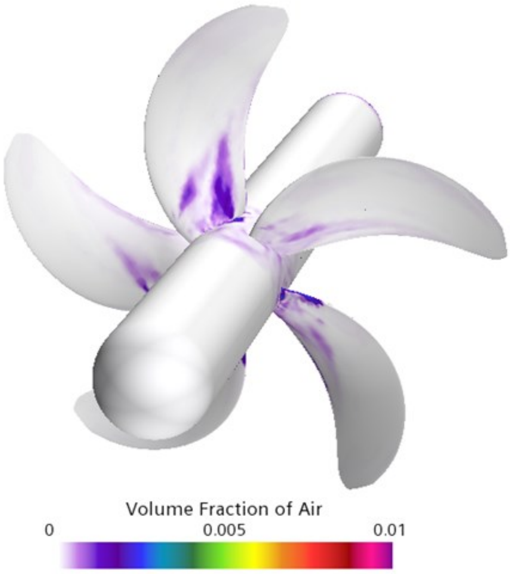

Figure 40: Volume fraction of air on the propeller geometry for the 1.169 m/s case 10 set-up.

Comparing the figures from the 0.997 m/s case 7 set-up and the 1.169 m/s case 10 set-up, there appear to be differences in the air volume fraction and distributions. The quantity of air being introduced and entrained beneath the plate is greater for the 1.169 m/s case 10 set-up, with a greater quantity of air reaching the propeller geometry. Furthermore, a greater quantity of air is being entrained in the propeller geometry itself in the 1.169 m/s case 10 set-up. The air distribution across the plate in the 1.169 m/s case 10 set-up also shows a greater width-wise distribution of air and a more established air layer. Tentatively, the comparison made here could point to a link between the quantity of air in the air layer, which subsequently impacts the quantity of air entrainment within the propeller, and the effect on propulsive characteristics.

The cases considered here have increased the air and water quantity concurrently, therefore maintaining the ratio of air quantity to water quantity stated in the 'as designed' condition. Overall, this simulation set has suggested that air ingress into the propeller can have a detrimental effect. However, this effect is highly variable, and at this stage, it would be inappropriate to draw specific conclusions or quantify the effect. It is again reaffirmed that this work should be taken as an indicative starting point for future work in experimental testing and other computational techniques. The possible deficiencies of the VOF modelling approach must again be highlighted. The immiscible assumption that VOF modelling utilises for the two phases limits the extent to which the multiphasic mixture can be represented, and this is brought into focus when considering a highly interpenetrating regime.

4.8 Supplementary pure air cases

Following the investigations carried out regarding the effect of varying the quantity of injected air in the air-water mixture, as well as the quantity of both air and water in the air-water mixture; it was considered a worthwhile continuation of the work to conduct an additional supplementary set of tests investigating the impact of injecting air exclusively, as is the case in some existing air lubrication systems. As this report focuses on air-water mixture systems such as the ARMADA system, considering a pure air regime was not in the primary scope. However, to prompt further work, a small simulation set was run at the highest global velocity (1.169 m/s), injecting differing quantities of air exclusively. The cases were run at mass flow rates ranging from 0.001 kg/s to 0.1 kg/s, and the results are shown in Figure 41.

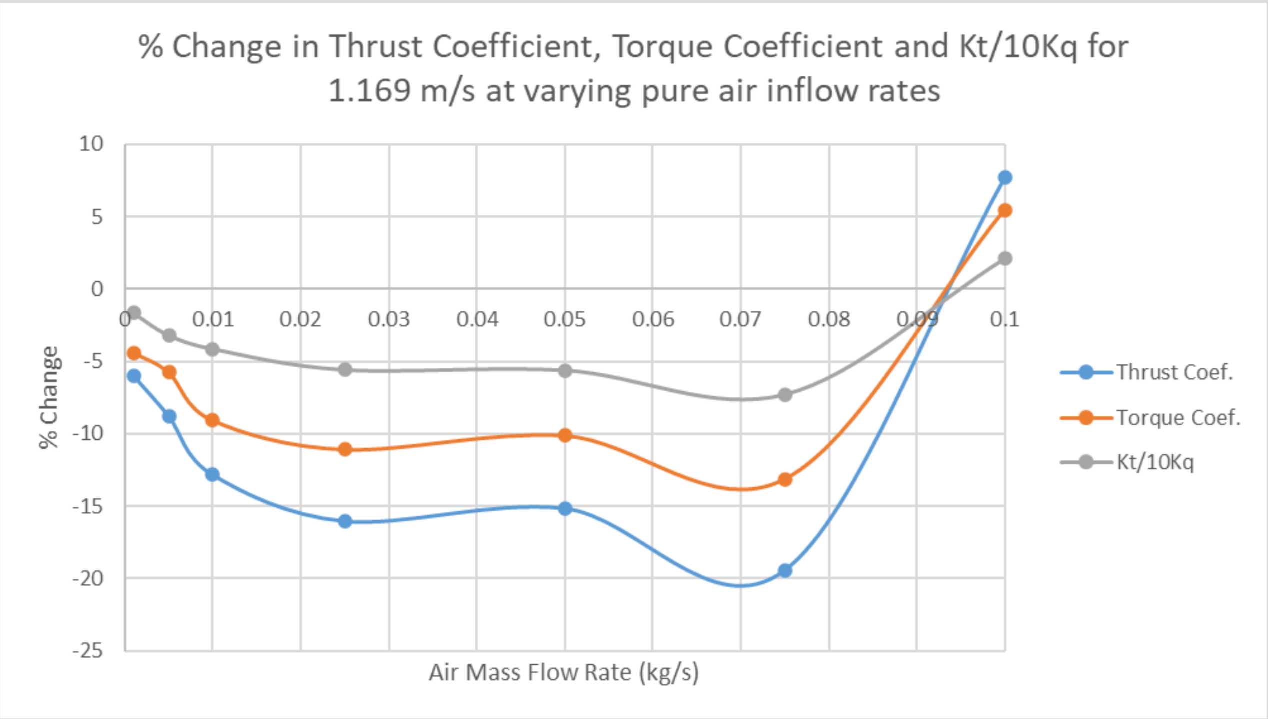

Figure 41: Pure air injection results for 1.169 m/s.

Although limited to investigating the effect under the 1.169 m/s condition, the results of these cases indicate the potentially notable impact that air ingress in the propeller can have upon propulsive characteristics. In all cases considered, thrust and torque coefficients have been impacted. Even at the lowest air injection rates below 0.01 kg/s, a decrease of up to around 12.5% was seen in the thrust coefficient and almost 10% in the torque coefficient. In the limited cases considered here, there exists a point where further air injection does not noticeably affect the reduction in thrust and torque coefficient. However, there appears to be a further decrease in the coefficients in the second-highest air injection case. Notably, in the 0.1 kg/s case, the effect on thrust and torque coefficient appears reversed. However, upon investigation of the simulation, it appears that at this highest air flow rate, the VOF approach's ability to resolve the air's behaviour and distribution was poor.

Therefore, the 0.1 kg/s case can be accounted for and is likely not indicative of the expected behaviour.

The ratio of Kt/10Kq can again be considered, and in these cases, this ratio generally follows the behaviour seen in thrust and torque coefficient. The ratio shows a 5 to 7% reduction for the intermediate air flow rates, with a lesser reduction at the lower injection rates. In the same manner as the previous multiphase cases, producing representations of the air distribution for this set of cases was possible.

These are shown in Figure 42 to Figure 44 and are from the 0.05 kg/s case.

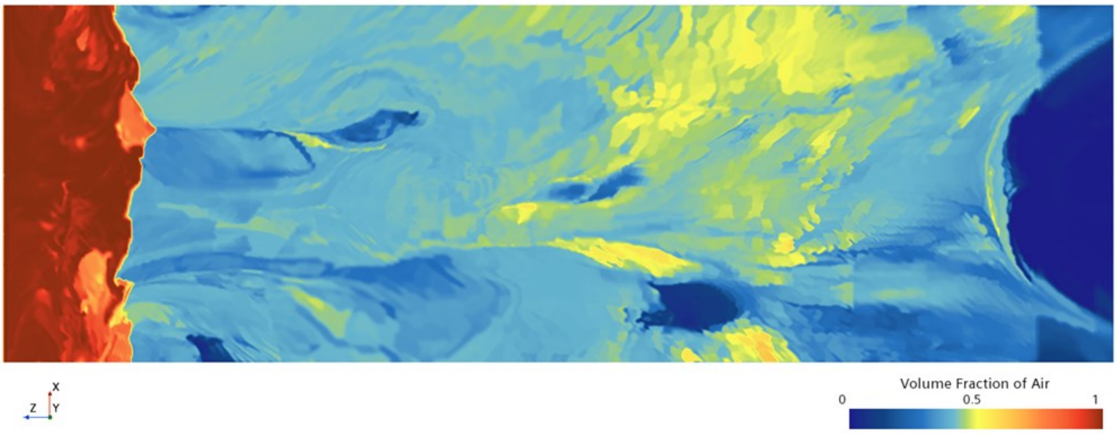

Figure 42: Volume fraction of air scene for the 0.05 kg/s case.

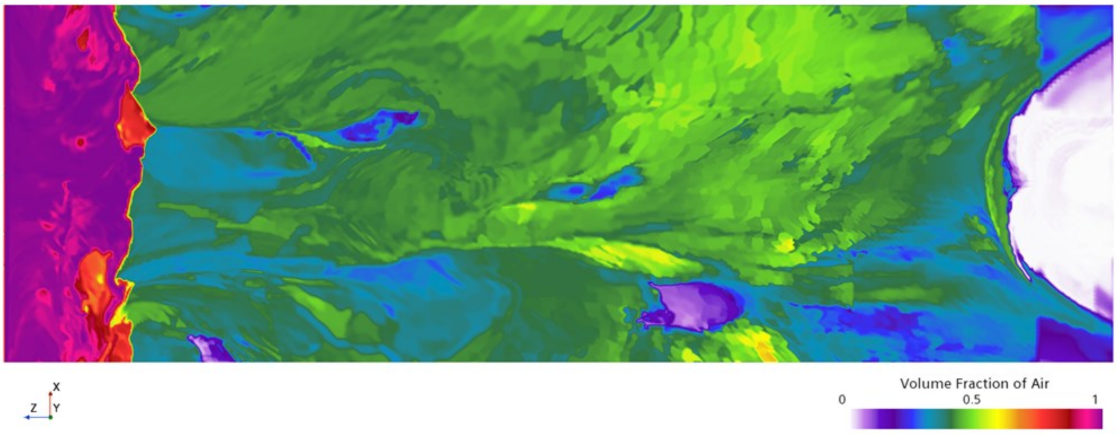

Figure 43: High contrast image for the 0.05 kg/s case.

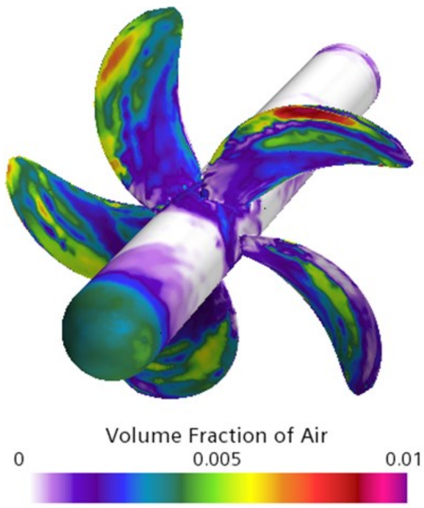

Figure 44: Volume of fraction of air on the propeller geometry for the 0.05 kg/s case.

It is apparent that the quantity of air constrained beneath the plate and the quantity of air entrained in the propeller is considerably higher than in the previous simulation sets. For Figure 42 and Figure 43, which represents the air underneath the plate; the volume fraction of air far exceeds the range seen in the previous simulation sets, as would be expected when injecting air exclusively. In Figure 44, the air entrained in the propeller is represented, and again, it is clear that the quantity of air entrained at the propeller wall is much higher in this case than in the previous simulation sets.

It must be reiterated that this set of simulations was carried out purely for supplementary purposes and to prompt further consideration and investigation regarding air-propeller interaction. Early indications from this supplementary work point towards a larger quantity of air and greater air coverage on the propeller surface, which could lead to more significant degradation of the propulsive characteristics. It is, however, inappropriate to draw clear conclusions from the results included in this data set before further investigation is completed.

5 Response surface methodology and input to surrogate models

As an additional element of this work regarding the impact of air ingress on the ship's propeller, Response surface methodology (RSM) has been utilised to assess the impact of the input parameters considered in this study on the thrust coefficient, which is the primary propulsive characteristic under consideration. The relevant parameters for the RSM work were the rate of water flow, the rate of air flow and the velocity.

The software Minitab was used to carry out the RSM work and has produced several useful outputs that can be utilised within surrogate models included in another section of the RETROFIT55 project, which focuses on developing a web-based decision support system tool. It is essential to note that this RSM work has been conducted based on the results of the limited cases examined in this study, as well as the quantity of air and water required to achieve the target drag reduction level. In preparation for the RSM work, the velocity, airflow and water flow were non-dimensionalised by changing the parameters into relative parameters (Relative to the 'as designed' condition). These parameters are shown in Appendix 1.

The regression equation for the work is presented below, along with its corresponding coefficients.

Regression equation

$$Relative\ Change\ in = -6.87 + 5.87\ Dimensionless\ Velocity + 0.244\ Dimensionless\ Water\ Flow\ + \\ + 0.169\ Dimensionless\ Air\ Flow$$

Table 7: Regression equation coefficients.

Coefficients					
Term	Coef.	SE Coef.	T-Value	P-Value	VIF
Constant	-6.87	1.55	-4.43	0	
Relative Velocity	5.87	1.29	4.55	0	1
Relative rate of water flow	0.244	0.155	1.58	0.121	1.25
Relative rate of air flow	0.169	0.172	0.98	0.33	1.25

5.1 Contour plots

The following contour plots in Figure 45, **Errore. L'origine riferimento non è stata trovata.** and Figure 47 were produced, showing the relation between each pair of parameters to the relative change in thrust coefficient.

The relative reduction in thrust coefficient indicates that with a higher positive value, the parameter has a larger detrimental effect on the thrust coefficient. With this in mind, it is clear from the contour plots that relationships exist between the studied parameters, and that differing combinations of these parameters can have varying effects. These effects will be discussed holistically with other factors as part of the reports in WP1. The response surfaces can help to elucidate future studies.

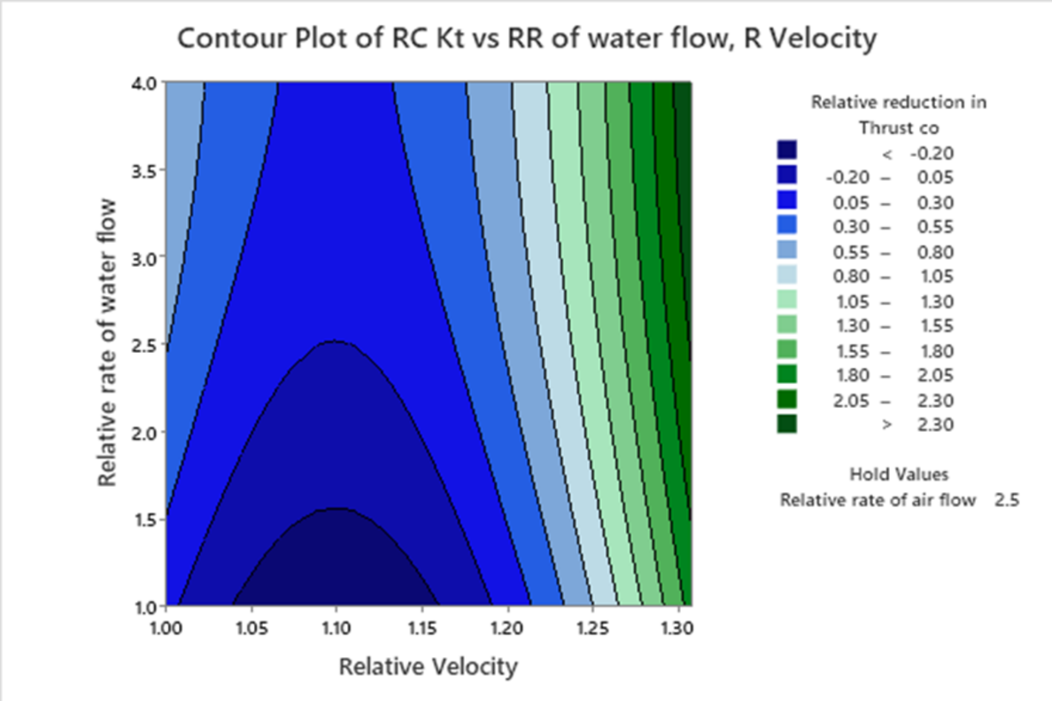

Figure 45: Contour plot of relative change in thrust coefficient vs relative rate of water flow and relative velocity.

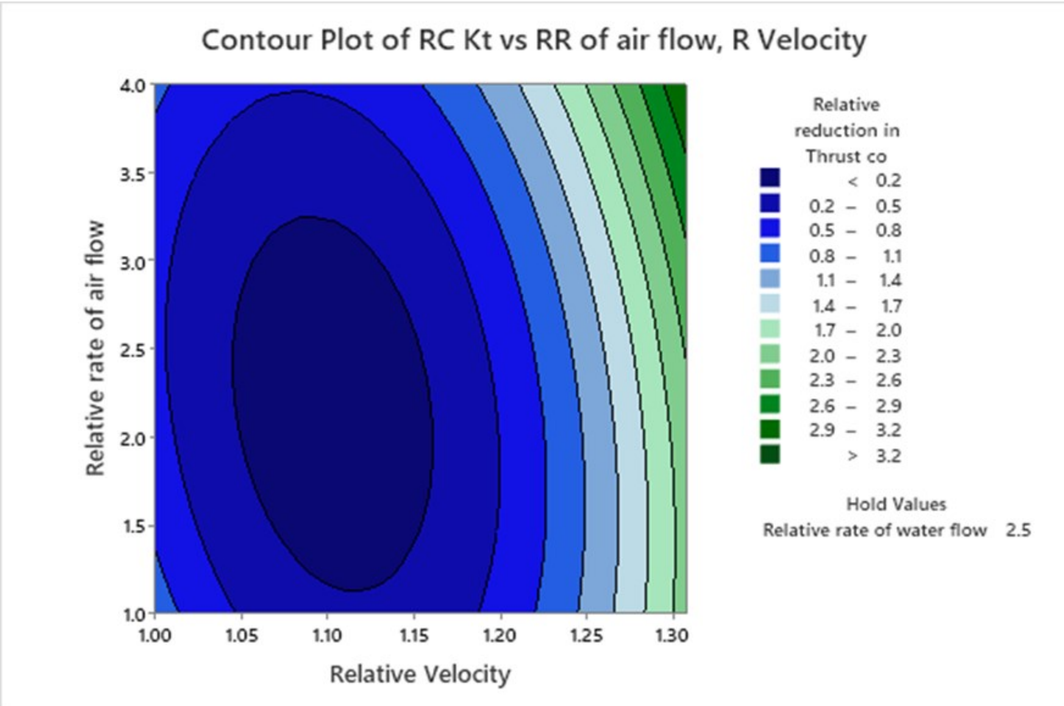

Figure 46: Contour plot of relative change in thrust coefficient vs relative rate of air flow and relative velocity.

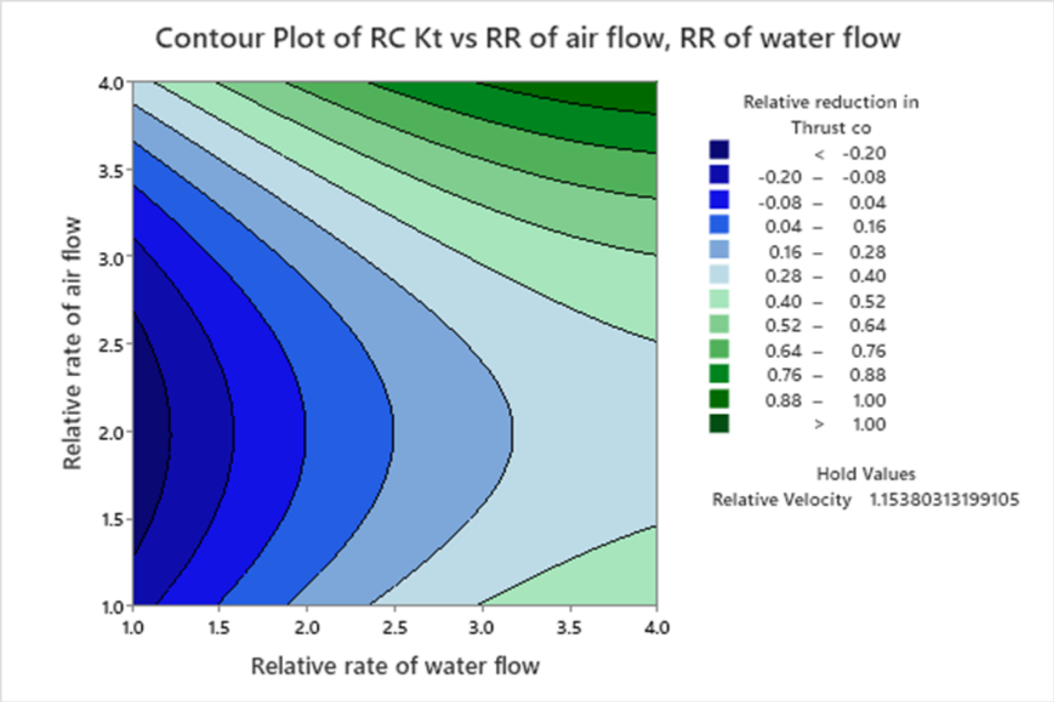

Figure 47: Contour plot of relative change in thrust coefficient vs relative rate of air flow and relative rate of water flow.

5.2 Surface plots

The following surface plots in **Errore. L'origine riferimento non è stata trovata.**, Figure 49 and Figure 50 were produced, further illustrating the relationship between each pair of parameters and the relative change in thrust coefficient.

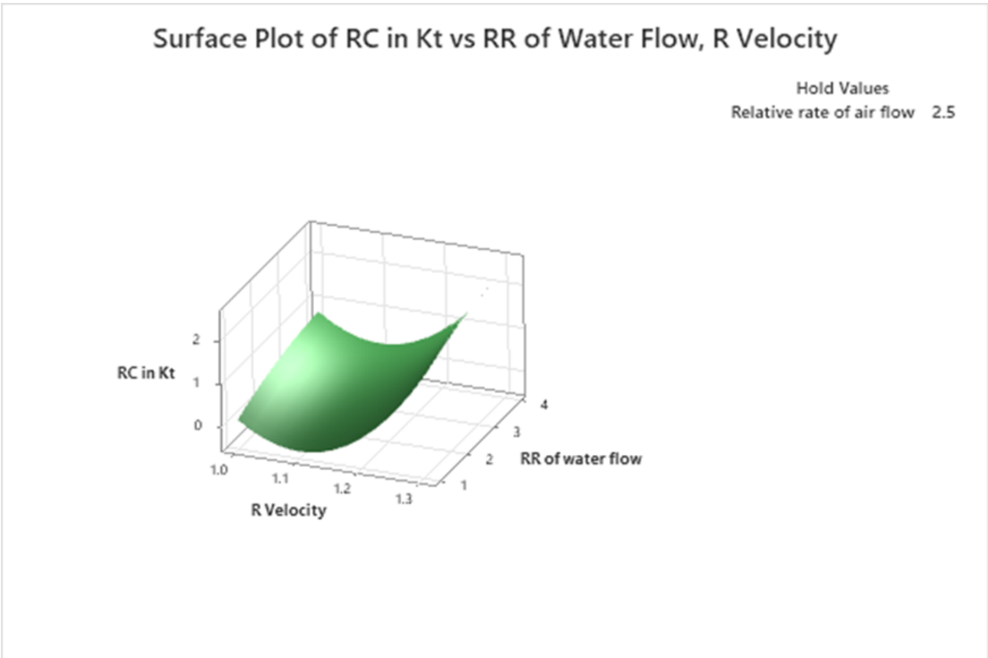

Figure 48: Surface plot of relative change in thrust coefficient vs relative rate of water flow and relative velocity.

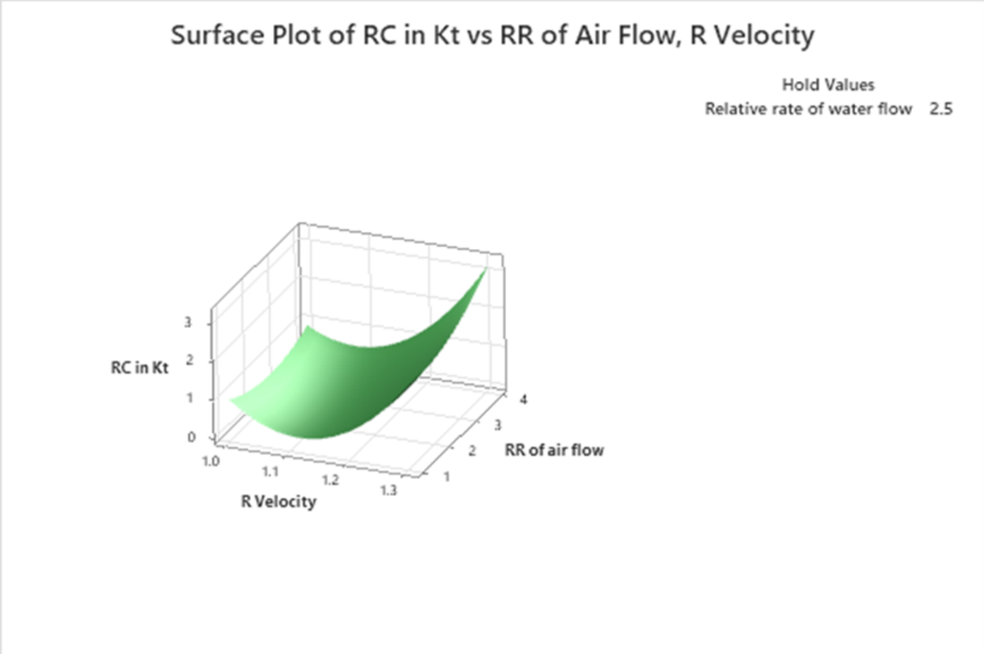

Figure 49: Surface plot of relative change in thrust coefficient vs relative rate of air flow and relative velocity.

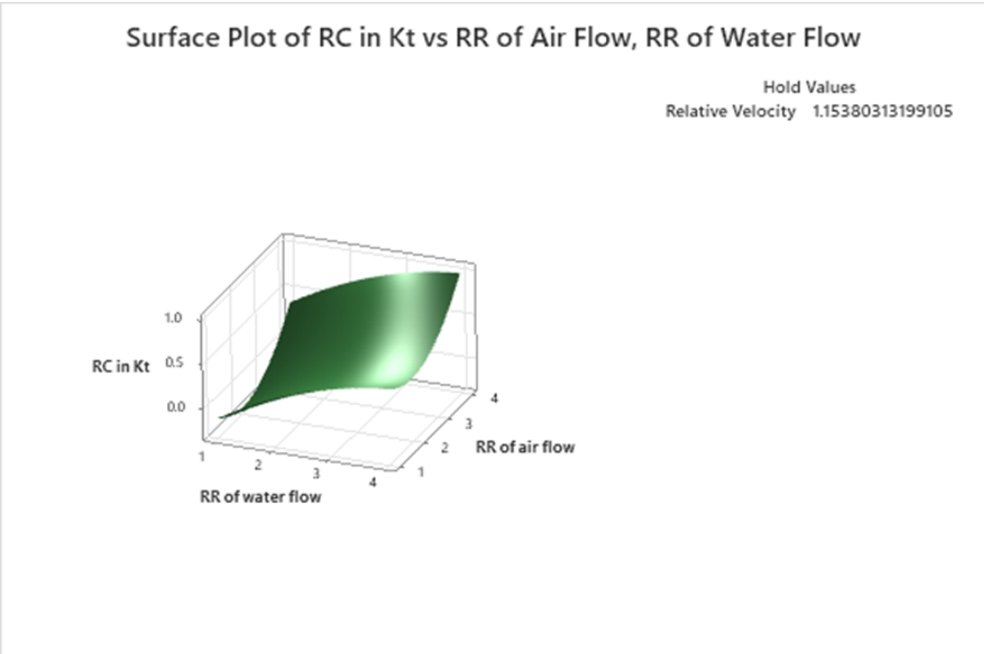

Figure 50: Surface plot of relative change in thrust coefficient vs relative rate of air flow and relative rate of water flow.

Again, these surface plots indicate relationships between the parameters. The relative reduction in thrust coefficient indicates that with a higher positive value, the parameter has a larger detrimental effect on the thrust coefficient. With this in mind, it is clear from the surface plots that relationships exist between the studied parameters and that differing combinations of these parameters can have varying effects, which will be discussed holistically with other factors as part of the reports in WP1. The response surfaces can help to elucidate future studies.

5.3 Factorial plots

Finally, factorial plots for the relative reduction in Thrust Coefficient were produced, showing the influence of each parameter on the mean of the relative reduction in thrust coefficient. This is shown in Figure 51.

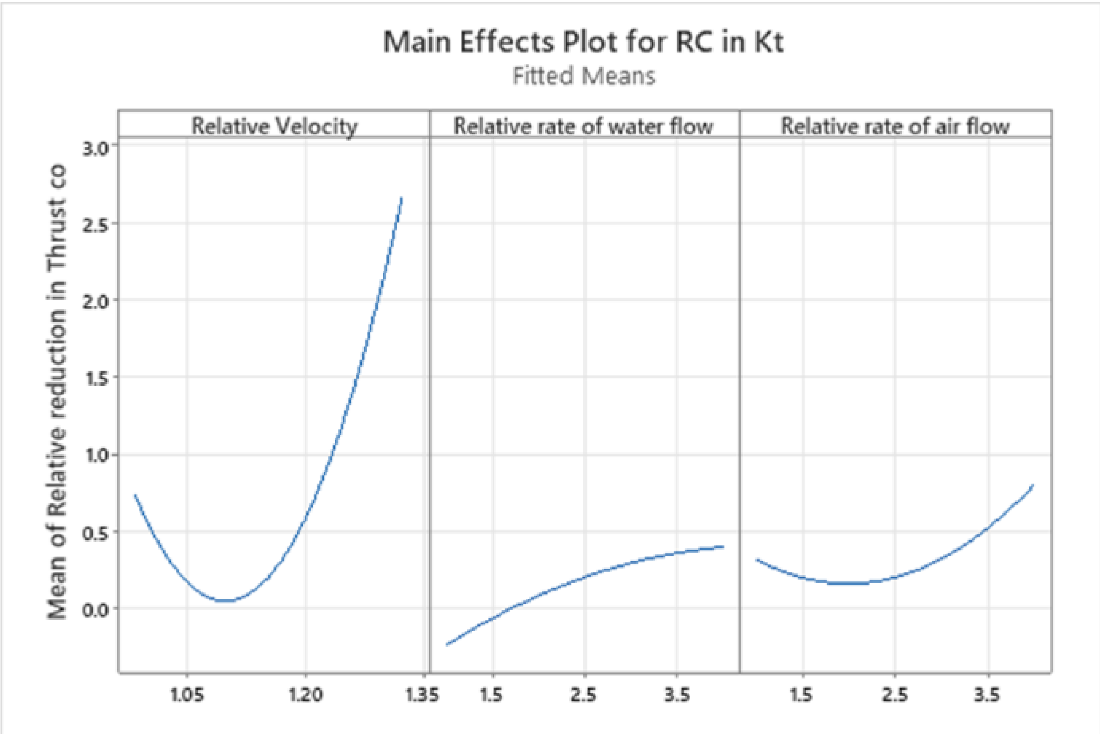

Figure 51: Main effects plot for relative change in thrust coefficient.

6 Concluding remarks

This report sought to investigate the potential impact of air ingress from utilising an air-water lubrication system. To investigate this potential impact, the work for the deliverable has focused on two approaches. Firstly, introducing the air as an air-water stream, and secondly, introducing the air via a slit in a plate.

In the first approach, a slight increase in efficiency is seen when the air-water stream is introduced. This is seen in the 90% mixture and the 95% mixture cases as opposed to the 100% (Pure water) cases. It is suggested that this results from lowering the mixture's viscosity in the cases considered. The representation of the air-water mixture as a stream varies considerably from what would be expected in reality. Moreover, the suitability of modelling one propeller blade in the periodic manner that was utilised must be considered further. The results of the first approach provide a useful indication of some of the propeller-mixture interaction behaviours that may be seen but must be accepted as having noted limitations.

In the second approach, there were three sets of simulation cases. Firstly, the 'as designed' condition cases were constructed to replicate the air injection system utilised in the towing tank tests as part of this project. Secondly, the air injection rate was adjusted away from the 'as designed' condition whilst maintaining the rate of water injected to investigate the effect of increasing air rate exclusively in the system. Thirdly, the water and air injection rate was increased to maintain the air-to-water ratio established from the 'as designed' condition and investigate the effect of increasing the overall combined flow rate for the system.

In most cases for the second (plate and slit) approach, some reduction in thrust and torque coefficient was seen. The ratio of Kt/10*Kq was used as a comparative element to indicate how torque is being transferred into thrust for the propeller. This comparative element was used instead of efficiency calculation due to the effects on propeller inflow, which were seen in using a plate in the simulation to constrain the air. The behaviour of the ratio varied as expected, dependent on the corresponding reduction in thrust and torque coefficient and how these related to each other.

Where a reduction in thrust coefficient is seen, this would indicate that the effect of air ingress compromises the propulsive characteristics of the propeller. A reduction in torque coefficient could indicate that the propeller requires less torque to rotate at the specified speed. However, given that the reduction in torque coefficient is seen with an accompanying decrease in thrust coefficient, this is not viewed as a positive indicator but instead as an indicator of deterioration in propulsive characteristics for the propeller.

There are some preliminary indications that increased air quantity entrained beneath the plate and subsequent increased air ingress and entrainment into the propeller may result in a more significant detrimental effect on the propeller's propulsive characteristics. It is, however, not appropriate to draw clear conclusions on this or the wider behaviour relating to air ingress. This is due to several factors. The approach utilised a VOF multiphase approach, where the air and water are viewed as immiscible fluids. This assumption is insufficient to model the behaviour of the air-water mixture fully. Therefore, although this work has provided pertinent areas for further investigation, it is concluded that further investigation utilising alternative simulation approaches would be necessary, as well as experimental testing to confirm the behaviours seen in this work.

Furthermore, and perhaps most pertinently, the air-water mixture is introduced directly into the propeller in this work's first and second approaches. In the first approach, this is done via the mixture being introduced as a stream, and in the second approach, the use of a plate constrains the air and directs the mixture into the propeller plane. Therefore, it must be clearly stated that the representations of the quantity of air ingress into the propeller in this work are an exaggeration of what would be witnessed in the practical application of this technology. However, as the extent of air ingress into the propeller depends on the choice of system, hull geometry and operational conditions, future work would benefit from a greater understanding of the expected quantity of air entering the propeller plane.

Finally, and in relation to further investigation, this work should be considered an indicative starting point for future work in experimental testing and other computational techniques. If the indications of this work are confirmed in further work, dependent on the air lubrication system utilised, ship hull design and operational conditions, air ingress could contribute to the overall effectiveness of air lubrication systems as a drag-reducing technology.

References

[1] ZEWT, *Executive summary realizing zero-emission*. 2023.

[2] Bogdevich, V., et al. *Gas-saturation effect on near-wall turbulence characteristics*. in *2nd Int. BHRA Fluid Drag Reduction Conf.;(United States)*. 1977.

[3] McCormick, M. and R. Bhattacharyya. *Drag reduction of a deep submergence vehicle by electrolysis*. in *Ocean 73-IEEE International Conference on Engineering in the Ocean Environment*. 1973. IEEE.

[4] McCormick, M.E. and R. Bhattacharyya, *Drag reduction of a submersible hull by electrolysis.* Naval Engineers Journal, 1973. **85**(2): p. 11-16.

[5] Kawabuchi, M., et al. *CFD Predictions of Bubbly Flow around an Energy-saving Ship with Mitsubishi Air Lubrication System*. 2011.

[6] Wu, H., Y. Ou, and Q. Ye, *Numerical study on the influence of air layer for propeller performance of large ships.* Ocean Engineering, 2020. **195**: p. 106681.

[7] Andrew Spiteri, H.R., Alex Routledge, Massimo Falchi, Emanuele Spinosa, Alesandro Iafrati, David Hitchmough, Onur Yuksel, Eddie Blanco Davis, Jin Wang, Stefan Harries, Roger Armson, *System design to deliver maximum drag reduction by PALS*. 2024, LJMU, FSYS, ARM, CNR: RETROFIT 55.

[8] Papadakis, G., *Development of a hybrid compressible vortex particle method and application to external problems including helicopter flows*. 2014, Εθνικό Μετσόβιο Πολυτεχνείο (ΕΜΠ). Σχολή Μηχανολόγων Μηχανικών. Τομέας ….

[9] Ntouras, D. and G. Papadakis, *A coupled artificial compressibility method for free surface flows.* Journal of Marine Science and Engineering, 2020. **8**(8): p. 590.

[10] Manolesos, M. and G. Papadakis, *Investigation of the three-dimensional flow past a flatback wind turbine airfoil at high angles of attack.* Physics of Fluids, 2021. **33**(8).

[11] Ntouras, D., et al. *Hydrodynamic response of a floating offshore wind turbine using an artificial compressibility finite volume method*. in *ISOPE International Ocean and Polar Engineering Conference*. 2023. ISOPE.

[12] LJMU, A. *Prospero Specifications*. 2024; Available from: https://prospero-docs.readthedocs.io/en/latest/specifications.html.

[13] Pineda-Pérez, H., et al., *CFD modeling of air and highly viscous liquid two-phase slug flow in horizontal pipes.* Chemical Engineering Research and Design, 2018. **136**: p. 638-653.

[14] Stenmark, E., *On multiphase flow models in ANSYS CFD software.* 2013.

[15] Hammer, T., et al., *Free fall drag estimation of small-scale multirotor unmanned aircraft systems using computational fluid dynamics and wind tunnel experiments.* CEAS Aeronautical Journal, 2024. **15**(2): p. 269-282.

[16] Khan, F., B. Batul, and A. Aizaz, *A CFD Analysis of Wingtip Devices to Improve Lift and Drag Characteristics of Aircraft Wing.* IOP Conference Series: Materials Science and Engineering, 2019. **642**: p. 012006.

[17] ITTC, *ITTC – Recommended Procedures: Testing and Extrapolation Methods Propulsion, Propulsor Open Water Test*. 2002. p. 9.

[18] ITTC, *ITTC – Recommended Procedures: Practical Guidelines for Ship Self-Propulsion CFD*. 2014. p. 10.

Appendix 1 – Relative parameters

Relative Velocity	Relative rate of water flow	Relative rate of air flow	Relative reduction in Thrust coefficient
1	1	1	1
1	1	1.5	1.599528815
1	1	2	1.031455716
1	1	2.5	0.057827997
1	1	3	0.484315167
1	1	3.5	0.496606045
1	1	4	0.543467825
1.115213	1	1	0.034541458
1.115213	1	1.5	-1.893898461
1.115213	1	2	-2.452183822
1.115213	1	2.5	-0.73747643
1.115213	1	3	-1.282060328
1.115213	1	3.5	-0.764292041
1.115213	1	4	0.293181546
1.192394	1	1	-0.061371821
1.192394	1	1.5	0.048063198
1.192394	1	2	-0.010116777
1.192394	1	2.5	-0.237856583
1.192394	1	3	0.941061383
1.192394	1	3.5	0.20394098
1.192394	1	4	1.471632303
1.307606	1	1	1.005689688
1.307606	1	1.5	3.330108118
1.307606	1	2	2.751262697
1.307606	1	2.5	2.359950616
1.307606	1	3	2.848864616
1.307606	1	3.5	0.974407274
1.307606	1	4	2.843574597

Relative Velocity	Relative rate of water flow	Relative rate of air flow	Relative reduction in Thrust coefficient
1	1.5	1.5	0.401975
1	2	2	-0.32756
1	2.5	2.5	-0.08725
1	3	3	0.639631
1	3.5	3.5	1.818549
1	4	4	-0.10916
1.115213	1.5	1.5	-0.40155
1.115213	2	2	-0.31735
1.115213	2.5	2.5	0.027644
1.115213	3	3	0.504864
1.115213	3.5	3.5	0.601038
1.115213	4	4	0.140905
1.192394	1.5	1.5	0.928017
1.192394	2	2	0.955804
1.192394	2.5	2.5	0.83707
1.192394	3	3	1.304589
1.192394	3.5	3.5	2.568247
1.192394	4	4	2.7221
1.307606	1.5	1.5	1.524084
1.307606	2	2	0.563974
1.307606	2.5	2.5	2.106807
1.307606	3	3	2.898422
1.307606	3.5	3.5	2.655278
1.307606	4	4	2.148638